ANODIC ALUMINA OXIDE AS HARD MASK FOR GRAPHENE NANOMESH FABRICATION

A thesis submitted to the Delft University of Technology in partial fulfillment of the requirements for the degree of

Master of Science

in Microelectronics, Electrical Engineering

by

Óscar Ortega González

September 2024

Electronic Components, Technology and Materials

Department of Microelectronics

Faculty of Electrical Engineering, Mathematics and Computer Science

Delft University of Technology, the Netherlands

Student Number:	5634806	
Project duration:	September 13, 2023 – September 23, 2024	
Thesis committee:	Dr. ir. S. Vollebregt	ECTM, Department of Microelectronics
	Dr. L.N. Sacco	ECTM, Department of Microelectronics
	Dr. Ivan Buijnsters	3mE, PME, Micro and Nano Engineering
	Prof.dr. P.J. French	BE, Department of Microelectronics

ACKNOWLEDGEMENTS

I would like to express my deepest gratitude to my thesis supervisor, Dr. Sten Vollebregt, who offered invaluable guidance and support in every single stage of this project. His feedback and encouragement throughout this journey were crucial to the successful completion of this thesis, for which I am extremely thankful.

I would also like to extend my sincere appreciation to my co-supervisors, Dr. Leandro Sacco and Dr. Ivan Buijnsters, for their dedicated mentorship. Their advice and involvement were a great aid in the realization of this research.

Finally, I am deeply grateful to my family for their unconditional support. Their generosity has given opportunity to pursue a career in a field I am passionate about. They are a constant source of motivation and encouragement.

ABSTRACT

Graphene, despite its exceptional electrical properties, is not suitable as a channel material in field-effect transistors due to its zero band gap. Engineered graphene structures, such as graphene nanoribbons, have been proposed to overcome this limitation. However, nanoribbons, while offering an opened band gap and favourable current on/off ratios, suffer from low individual driving currents. Graphene nanomesh provides a potential solution by maintaining the benefits of nanoribbons while offering higher driving currents due to its two-dimensional structure. However, fabricating graphene nanomesh remains challenging.

This study investigates the fabrication of graphene nanomesh using a transfer-free anodization method with nanoporous anodic alumina as a hard mask in a plasma etching process. Unlike previously published methods, which require the transfer of brittle alumina masks, this work develops a process where anodization is performed directly on aluminium deposited on top of graphene. A two-step anodization process was tested and optimized using aluminium on silicon samples, including the development of a partial stripping variation aimed at preserving pore ordering.

Initial tests on Al-on-Si samples demonstrated promising results, with plasma etching yielding uniform patterns when using the partial stripping technique. However, when applied to graphene samples, significant challenges were encountered. Poor adhesion between aluminium and graphene layers resulted in delamination and bubbling during anodization, disrupting the pore formation process and leading to defects. Efforts to improve adhesion through patterning of the substrate showed no substantial improvements. However, it was confirmed that the Mo and the graphene survived the anodization process.

Although plasma etching produced positive results in regions where delamination was minimized, etching on graphene samples remained inconsistent. Despite these challenges, the study provides valuable insights into the fabrication process, particularly regarding mask stability and adhesion issues.

CONTENTS

1 INTRODUCTION 1
1.1 Motivation and problem formulation 1
1.2 Thesis objectives 2
1.3 Thesis outline 2
2 BACKGROUND THEORY AND LITERATURE REVIEW 3
2.1 Anodic alumina oxide 3
2.1.1 Porous anodic alumina 3
2.2 Graphene synthesis 9
2.2.1 Mechanical exfoliation 9
2.2.2 Liquid phase exfoliation 9
2.2.3 Chemical Vapor deposition 10
2.2.4 Graphene oxide reduction 11
2.3 Material Characterization 12
2.3.1 Raman spectroscopy 12
2.3.2 Scanning electron microscope (SEM) 13
3 EXPERIMENTAL METHODOLOGY 16
3.1 Full process flowchart 16
3.2 Grapehene growth 17
3.3 Anodization 18
3.3.1 Anodization Setup 18
3.3.2 Anodization conditions 26
3.3.3 Electrolyte maintenance 27
3.3.4 Anodization tests – Establishing anodization speed 28
3.3.5 Anodization tests - Stripping process 29
3.3.6 Two-step anodization optimization 31
4 RESULTS AND DISCUSSION 42
4.1 CVD-grown graphene 42
4.2 Anodization on graphene 43
4.3 Plasma etching 46
4.3.1 Aluminium on silicon samples 47
4.3.2 Graphene sample 49
5 CONCLUSIONS AND RECOMMENDATIONS 54
5.1 Future work 55
6 BIBLIOGRAPHY 56

1 INTRODUCTION

1.1 Motivation and problem formulation

Graphene is a one-atom thick two-dimensional layer of sp2 -hybridized carbon and has been the focus of numerous research since its experimental discovery in 2004 [1]. This nanostructured material has received a lot of attention due to its incredible electrical, mechanical, and chemical stability properties.

In the field of field-effect-transistors (FETs), the use of graphene could be very interesting to explore as MOSFET scaling is reaching its limits. The novel characteristics of this material could be the answer to keep improving the performance of transistors. Its high conductivity and 2D structure make it very appealing to use for single back-channel devices with good electronic properties.

However, the use of graphene in field-effect-transistors (FETs) has been limited. The main enemy in the battle of implementing graphene in single back-channel devices has been its bandgap. Due to the 0 eV bandgap in low-defect graphene [2], a FET device with this material as a channel could not be turned off at room temperature. Nonetheless, the band gap of graphene can be modified and increased. This can be achieved by doping, hydrogenating, or fabricating graphene-based nanostructures such as graphene nanoribbons (GNR).

Graphene nanoribbons are thin strips of graphene sheets cut along a certain orientation of the graphene crystal plane. GNRs have tuneable bandgaps that depend on the width of the strip [3], and with the right size, they have shown in the past to have great current ON/OFF ratios that are sufficient for transistor operation [4], [5]. Unfortunately, their individual driving current and conductance are very low and a dense array of them would be needed to use them in practical applications. To fabricate such arrays, costly and low-throughput methods such as electron-beam lithography are currently required [6], [7], so their use in the industry would not be justifiable at the present time.

With the aim of solving this issue, a new graphene-based nanostructured known as graphene nanomesh (GNM) was synthesized [8]. GNM is a single or multiple layer graphene sheet with nanoholes punched out following a periodic and regular pattern. This structure has shown to have driving currents of almost 100 times larger than those obtainable with single nanoribons. However, the main methods that can be used for its fabrication, such as block copolymer lithography [8], and nanosphere lithography [9], rely on reactive ion etching using toxic gases in order to remove SiO_2. Other techniques such as nanoimprint lithography has been successfully used [10], but the template preparation process is challenging.

In hopes to finding better fabrication methods for GNM, some research groups have shifted their attention to nanoporous anodic alumina (NAA). NAA is a material that presents a honeycomb-like structure with pore sizes that can be tuned depending on the anodization conditions used. It is obtained through the electrochemical oxidation of aluminium, which makes its production scalable and inexpensive. In 2012, this material was tested as a mask for a GNM fabrication process [11]. A membrane of alumina of 1um thickness was fabricated separately from a high purity aluminium foil. The membrane was then transferred on top of

reduced graphene using poly(methyl methacrylate) (PMMA) as an adhesion layer. Finally, the reduced graphene was patterned into a GNM after an oxygen plasma etching process.

While the study yielded positive results, the quality of the obtained GNM was found to be very dependent on having a perfect interface between the layers, and on having a low, even thickness of that PMMA layer. Adhesive layer thicknesses larger than 8nm lead to areas of the graphene sheet being etched with large holes fused together, and other areas not being etched at all. The simplicity of this technique shows promise, but some of the steps required to do the layer transfer still make the use of NAA as a hard mask challenging.

1.2 Thesis objectives

In the present work, the fabrication of GNMs with NAA as a mask using a transfer-free method is explored. Instead of fabricating the alumina separately and then transferring it on top of graphene with the help of a thin PMMA layer, a process that can damage the membrane due to the brittleness of the material, the alumina layer is grown on top of the graphene directly. This involves depositing a thin aluminium layer on a wafer with CVD-grown graphene, performing anodization on the die, and then etching the graphene with oxygen plasma using NAA as the mask. The aim of this work is to simplify the previously tested fabrication methods and improve the quality and scalability of GNM production.

1.3 Thesis outline

The thesis is comprised of five chapters:

· **Introduction**: this chapter presents the motivation behind this work and the objectives set for the thesis.

· **Background theory**: this chapter summarizes the fundamental concepts, and latest research outcomes on nanoporous anodic alumina and graphene synthesis.

· **Experimental methodology**: this chapter focuses on explaining the methodology used to producing the results. The technique chosen to synthesize graphene is explained, as well as the anodization processes followed. The most extensive section of this chapter is the anodization one, where the set up used for anodization is presented in detail, as well as all the steps followed to optimize the anodization process.

· **Results and discussion**: this chapter presents the main findings of the research. The characterization methods are explained, and the results from the processes followed in the previous chapter are displayed and discussed.

· **Conclusions**: this chapter reflects on the results found, summarizes the work, and proposes improvements for future work.

2 BACKGROUND THEORY AND LITERATURE REVIEW

In this chapter, a detailed explanation is given about the background theory of this thesis. For the realization of this work, three main subjects were studied: nanoporous anodic alumina formation, graphene growth, and patterning with alumina as a mask. All three of these subjects were researched in depth and the different approaches for all of them found in the literature were examined. This was done to firstly understand the science behind the phenomena involved, and, secondly, to select the best approach for the present work. In this section, a summary of all the relevant information about these three subjects is presented.

2.1 Anodic alumina oxide

The electrochemical oxidation of metals leads to the formation of an oxide layer on the metal's surface, a phenomenon known as anodization. This process has been extensively investigated across various metals, including iron, copper, gold, titanium and more. In the case of aluminium, anodization results in the formation of anodic alumina oxide.

Anodic alumina oxide exists in two distinct forms, primarily influenced by the type of electrolyte utilized during anodization: a solid form and a porous form. When aluminium is subjected to a neutral or alkaline electrolyte environment, that is when the electrochemical oxidation yields a solid layer of aluminium oxide. This layer can grow until a maximum thickness is reached. This occurs when the ions involved in the process can no longer diffuse through the oxide layer for a given potential. On aqueous electrolytes, the highest potential that can be reached before breakdown occurs is about 1000V. This voltage corresponds to an oxide layer of approximately 1 µm.

The aim of this work is to use the self-ordered nanoporous pattern of alumina as a hard mask. For that reason, from this point onward, the solid form will not be discussed in more detail, and only the nanoporous form will be examined.

2.1.1 Porous anodic alumina

When anodization is carried out in an acidic environment {usually sulfuric (H2SO4), oxalic (H2C2O4), or phosphoric (H3PO4) acids} under potentiostatic (constant voltage) or galvanostatic conditions (constant current), porous alumina can be obtained. What makes the formation of pores possible under these conditions is the fact that alumina oxide is soluble in acidic electrolyte. That solubility together with the right combination of anodization parameters, leads to the growth of self-ordered pores that arrange themselves in a regular honeycomb pattern.

2.1.1.1 Formation process stages

The process of formation is divided into four distinct stages. In the first stage, a solid oxide layer is formed just like it would for the solid form alumina under alkaline or neutral conditions.

Subsequently, at stage 2, due to the solubility in acidic electrolyte, pores start to nucleate on the surface of the alumina, and the solid oxide layer starts to breakdown. In stage 3, the pores continue growing. Finally, in stage 4, self-ordering occurs, and the pores start to slowly rearrange to a form a more regular pattern.

In potentiostatic conditions, each of those stages can be identified by the change of current density in a plot over time. Figure 1 shows a typical current density-time curve for anodization under those conditions. During the first stage, current density decreases as the solid layer grows. Once the pore nucleation starts, current density reaches a local minimum and increases. Current density increases during the entire process of pore growth until it reaches a local maximum. From that point forward, a small decrease can be appreciated. That very mild decrease is caused by the last stage, as pores slowly self-order throughout the surface.

It is important to note that in galvanostatic conditions, the stages would occur similarly and in the same order. The choice between potentiostatic or galvanostatic conditions does not have an impact on how the process takes place. However, if the aim is to grow pores with a constant pore diameter, the constant voltage mode is usually employed, as that parameter is one of the main parameters that control pore size. How that anodization parameter, as well as the rest of them, affect the process and the pore morphology exactly, will be explored in more detail in a later section.

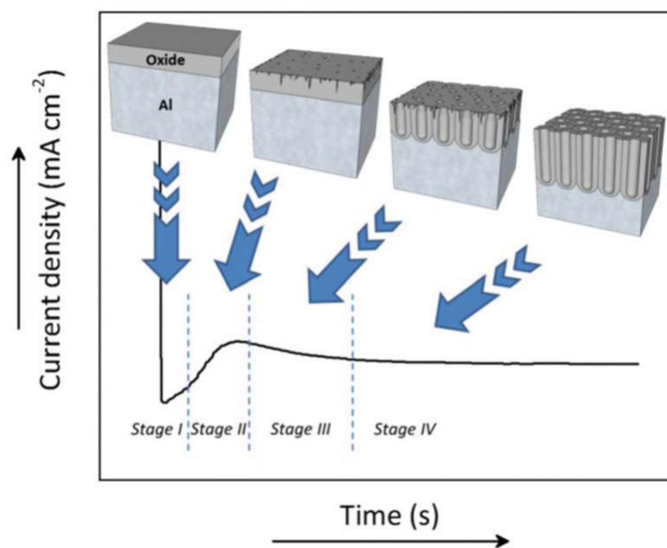

Figure 1: Profile of the typical current density-time curve recorded during potentiostatic anodization [12]

2.1.1.2 Pore mechanism

The process of pore nucleation is not fully understood as of today. Two main theories have been proposed to explain why pores might start forming from a solid aluminium oxide layer. The first one is known as the *field-assisted* model. This theory was developed by O'Sullivan and Wood [13], and it suggests that pore formation occurs when imperfections in the original barrier layer

cause different current concentrations, which, in turn, cause the oxide layer to grow non-homogenously. Pore nucleation points form at the thinner regions of the layer.

The other theory is known as the stress-driven mechanism. This theory was proposed by Shimizu and Thompson [14], and it suggests that stress created at the metal/oxide interface when the oxide layer grows is the cause of the pore nucleation. As tensile stress develops in the interface due to the volume expansion of the oxide layer forming, cracks appear in the layer. When a crack is formed, the layer experiences very high current density locally, which causes the metal near that point to be consumed to heal that region. That process results in the non-homogenous growth of the oxide layer and pore nucleation.

As of the writing of this work, the field-assisted model is the most accepted and cited theory of the two.

2.1.1.3 Pore parameters and anodization conditions

The anodization is controlled by four main parameters: anodization voltage, anodization time, electrolyte composition and temperature. Depending on the value of those parameters, the morphology of the porous honeycomb structure varies. In this section, the main geometrical features of porous anodized alumina oxide are explained, as well as the principal anodization parameters that are involved in their tuning.

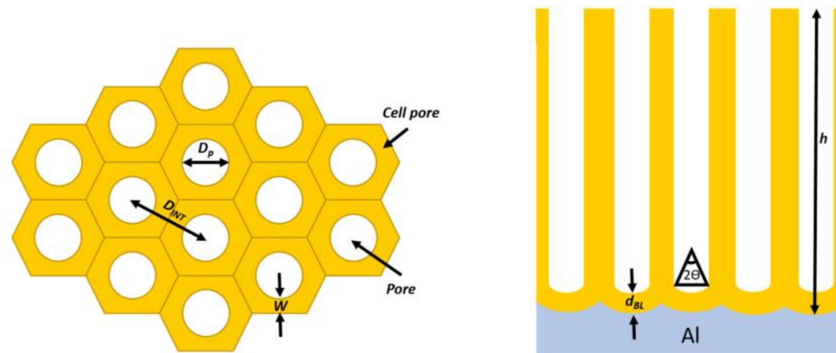

Figure 2: Schematic representation of main geometrical features of nanoporous alumina oxide [15]

In Figure 2, a schematic representation of the main geometrical features of porous alumina oxide can be found. The main features are the pore diameter (Dp), interpore distance (Dint), and barrier layer thickness (Dbl).

Anodization potential

It has been studied and demonstrated that all three of these features have a linear relationship with the anodization potential [13], [16], [17]. Higher potentials generate higher currents, and, as a result, bigger features are formed. Due to how clear this correlation is, potential is one of the primary ways of how the honeycomb morphology can be tuned and configured. However, it is important to note that for each of the most commonly used electrolyte compositions (0.3 M oxalic acid, 0.2 M sulfuric acid, and 0.3 M phosphoric acid), there is an ideal value of potential for which the maximum degree of pore ordering is achieved. Those values are 40, 25 and 195 V respectively for each kind of electrolyte. These values were found on optimization studies that

compared pore ordering degree for multiple achieved for different concentrations and potentials applied [18], [19], [20].

Therefore, while anodization is possible at other potentials, the ordering degree will vary depending on the electrolyte chosen and how distant the voltage picked is to the optimum value of that electrolyte.

When anodization is done near the optimum potential values for each electrolyte described in the previous paragraph, that is known as the mild anodization regime. On the other hand, when the potential used is considerably higher than the ideal potential, and it goes above the breakpoint of the oxide, then the anodization takes place in hard anodization conditions. Working in the hard anodization regime can be advantageous. High current densities allow for very fast growth speeds compared to mild anodization. Additionally, due to the linear dependence between potential and pore size still being in effect, larger features can be achieved under these conditions. However, these advantages come at a cost. Anodizing above the oxide's breakpoint, the oxide membrane is prone to burning and cracking. To counter these problems, methods such as improving heat dissipation by adding ethanol to the electrolyte can be used [21], [22].

Temperature

The effects of temperature on the honeycomb morphology are unfortunately not as clear as for anodization potential. Depending on the electrolyte used, different conclusions have been drawn on its effect in different studies [13], [23], [24]. These discrepancies have made it challenging for a common understanding to be reached on how this parameter influences pore morphology. However, something that is widely accepted and understood about temperature, is its influence on reaction rate. Anodizing at higher temperatures leads to higher current densities, which lead to a faster oxide growth rate. When high a degree of control is required for the final oxide thickness, temperatures close to 0 degrees Celsius might be the best choice. On the other hand, when a very thick layer is desired, choosing temperatures close to ambient temperature is most likely better to prevent very long anodization times.

Electrolyte composition

Different electrolytes can be used to obtain self-ordered nanoporous alumina. As previously stated, the three main ones that are used the most are 0.3 M oxalic acid, 0.2 M sulfuric acid, and 0.3 M phosphoric acid. These three acids have all been studied and tested extensively and they have shown a wide range of anodizing conditions for which self-ordered pores can be achieved. The choice of which one to use is mostly determined by the desired final pore diameter and interpore distance. Again, as previously discussed, the three acids have an ideal anodization potential for which they produce the best pore ordering (40, 25, and 195V). Therefore, working with phosphoric acid will be the best choice to achieve high degree ordering for large pores (between 150 and 200nm of Dp commonly) [17], [20], while using sulfuric acid will be best for high degree self-ordering of smaller pores (between 15 and 30 nm) [19], [25]

Other acids besides these three have been used in anodic alumina anodization. Acids such as arsenic [26], selenic [27], and chromic [28], among others, have been used to successfully produce self-ordered nanoporous oxide layers. However, none of these electrolytes have been

studied as thoroughly as the main three, and for that reason, as of today, the known conditions for which high ordering can be achieved with them are rather limited.

2.1.1.4 Two step technique

As discussed in the previous section, once the pores have nucleated and have fully formed, they start to self-order in the fourth stage of the anodization process. However, the self-ordering occurs at the oxide metal interface, and the pores that first nucleate at the surface of the aluminium remain scattered in a random pattern. If the aim were to obtain a thin layer of ordered nanoporous alumina to use as a mask, a regular anodization process would not be adequate.

That is the problem that Masuda et. al. [18] faced when they were exploring the possibility of using nanoporous alumina oxide as an evaporation mask to fabricate a nanogold array. A modification to the process was needed to be able to produce thin membranes with ordered pores all the way through. That is when they developed a method that would become an essential innovation: the two-step anodization process.

What Masuda and the rest of the team of researchers found out, is that by doing a long period anodization (10h in 0.3 M oxalic acid at 40V and 17ºC), then striping the oxide in a wet etching process (14h in 0.4 M phosphoric acid and 0.2 M chromic acid), and then doing a second anodization under the same conditions, the second layer of nanoporous oxide grows already ordered. This order that occurs immediately results from the surface of the aluminium being pretextured after the first anodization. When the first layer of oxide is removed, the bottom of the pores at the metal/oxide interface leaves an imprint on the metal. It is this imprint left by the first anodization that causes the pores of the second anodization to start growing ordered. Effectively acting like a template, pores are encouraged to grow from the preexisting topography that shares the same parameters due to the anodization conditions of the two anodization steps being identical.

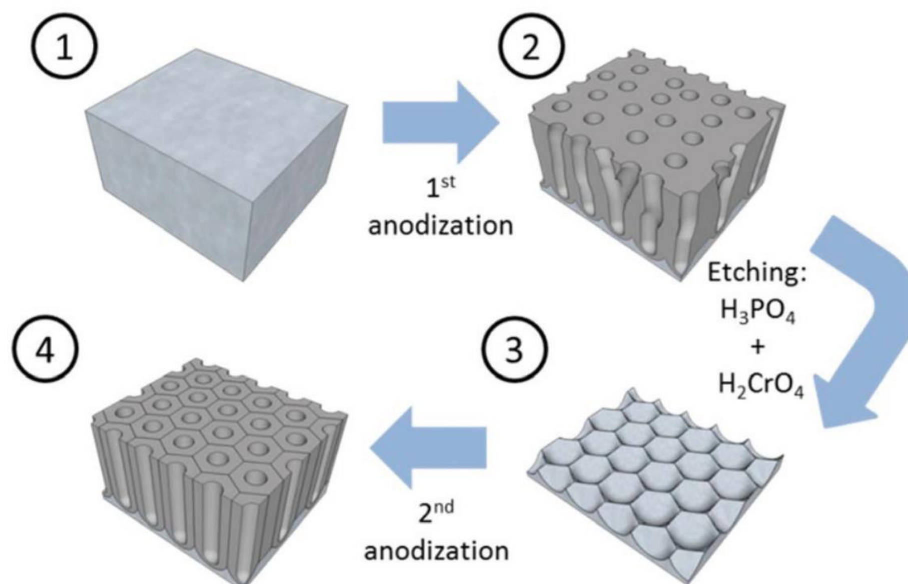

Figure 3: Schematic sketch of the two-anodization process developed by Masuda et al. to obtain thin layers of highly ordered nanoporous alumina [ref]

2.1.1.5 Conclusions on how to obtain high-ordered pores for this work

To achieve high pore ordering in porous anodic alumina, several key anodization strategies should be employed. First, it is essential to conduct anodization under potentiostatic conditions, meaning the voltage must remain constant throughout the process. Fluctuations in potential can lead to variations in pore diameter, which are undesirable for achieving uniformity across the membrane. Therefore, maintaining consistent anodization conditions is crucial.

The two-step anodization process is recommended for producing a nanoporous alumina layer suitable for use as a mask in dry etching. This process involves a long initial anodization followed by a shorter second one, with a stripping step in between. The first anodization should be extended as much as possible, as longer times have been shown to improve pore regularity, resulting in larger domains of perfectly ordered pores [23]. This enhances the quality of the pores formed during the second anodization.

Mild anodization conditions are preferred over hard anodization due to the reduced risk of issues such as oxide cracking and bubbling. Although mild anodization has a slower reaction rate, it is more reliable and has been extensively studied, with well-defined parameters that maximize pore regularity. This approach simplifies the process setup and is sufficient for a proof-of-concept study.

Finally, the anodization parameters should align with the optimal conditions identified by Masuda et al., who found that specific combinations of voltage and electrolyte composition—such as 40V with 0.3M oxalic acid, 25V with 0.2M sulfuric acid, or 195V with 0.3M phosphoric acid—yield the best pore ordering under mild anodization conditions. These parameters should be adopted to achieve the highest quality self-ordered alumina layer possible.

2.2 Graphene synthesis

The synthesis of graphene has undergone significant advancements in recent years, leading to several main methods that are widely employed today. This section aims to provide a comprehensive overview of the main ways graphene can be synthesized as of today.

2.2.1 Mechanical exfoliation

One of the earliest and simplest methods for graphene synthesis is mechanical exfoliation, commonly referred to as the "Scotch tape" method. This technique was first demonstrated by Novoselov and Geim in 2004 [1], and involves peeling off layers of graphite repeatedly using adhesive tape until FLG or SLG is obtained.

The simplicity of this top-down method where the graphene is extracted from a piece of graphite, allows the production of flawless monocrystalline graphene. It is for this reason that it has often been the preferred choice in fundamental research. Most new graphene properties and potential applications in prototype devices have been uncovered using mechanically cleaved flakes. Despite the ease of production and great quality, this method has major challenges when it comes down to scalability and the size of the sheets produced.

2.2.2 Liquid phase exfoliation

Liquid phase exfoliation (LPE) is another widely used top-down method for synthesizing graphene. The basic principle involves dispersing graphite in a liquid medium and then applying energy to separate the graphite layers into individual graphene sheets. Initially, graphite, composed of stacked layers of graphene, is introduced into a solvent. Common solvents include N-methyl-2-pyrrolidone (NMP) and dimethylformamide (DMF) [29], [30], [31]. These are chosen for their ability to stabilize graphene in suspension due to their surface energies matching that of graphene. Alternatively, water with surfactants or polymers can be used to prevent re-aggregation of graphene sheets by surrounding the graphene layers and reducing surface tension.

Energy is then applied to the graphite dispersion through sonication (using ultrasonic waves) or high-shear mixing. Sonication involves using ultrasonic probes or baths to create cavitation bubbles in the solvent, which collapse and generate high shear forces. High-shear mixing uses rotor-stator devices to produce intense shear forces. These forces overcome the van der Waals forces holding the graphite layers together, and it peels them apart into thin graphene sheets.

The resulting mixture contains a variety of exfoliated materials, ranging from single to few-layer graphene and unexfoliated graphite. Centrifugation is employed to separate these based on their size and density. By carefully selecting the centrifugation speed and time, monolayer and few-layer graphene can be isolated from the thicker particles.

LPE is scalable and can be performed in large batches [32], making it suitable for industrial applications. The graphene produced is of high quality, with relatively few defects, maintaining the intrinsic properties of graphene. The main challenge with this technique has to do with the lack of control of the sizes of the sheets produced. Be it with, surfactants, polymers or ionic

liquid systems, longer processing times lead to higher concentrations of graphene. However, longer times generate more defects and reduce the mean size of the sheets. A balance point is always needed to be found. Despite that, in summary, liquid phase exfoliation is a practical and efficient top-down method for producing high-quality graphene on a large scale at a moderate cost.

2.2.3 Chemical Vapor deposition

Chemical Vapor Deposition (CVD) has emerged as a leading technique for scalable graphene synthesis [33]. In CVD, a graphene sheet is grown from precursors in a high-temperature furnace with the help of specific transition metals (typically Ni or Cu) [34] that act as a substrate and a catalyst. The process begins with an annealing step, where the metal is heated to clean its surface and rearrange its crystalline morphology. This is done to increase the grain size of the lattice on the surface, in hopes of improving the quality of the graphene sheet that will later be grown on top of it. In the next step of the process, the precursors are introduced into the hot furnace and the reaction with the catalyst takes place. Depending on the solubility of the catalyst, one of two types of mechanisms will occur. If carbon is soluble in the catalyst, such is the case for Ni, then the atoms of carbon will dissolve into the bulk after precursor decomposition. When this type of mechanism takes place, graphene growth will not happen until the next step of the process. The other possible mechanism occurs when carbon is not soluble in the catalyst, such as with Cu. In that case, as the carbon atoms cannot migrate into the bulk, they will adsorb to the surface and start forming a graphene sheet directly.

Finally, in the last step, the furnace is cooled back down to room temperature. The atmosphere is the same inert one used for the annealing step, as otherwise, the graphene would functionalize with oxygen-containing groups when exposed to air at a temperature above 200ºC. If the substrate used is a high solubility one, it is at this point when the graphene sheet is formed. As the temperature decreases, the dissolved carbon atoms segregate from the bulk and attach to each other. For this type of substrate, cooling step dynamics are crucial as the amount of layers obtained and the growth process depend heavily on them. On the other hand, if the substrate used is a low solubility one, the sheet already formed in the previous step by adsorption, and a monolayer will be preferably grown as no segregation from the bulk occurs.

Figure 4 shows a representation of the growth kinetics that take place in the growth of graphene with CVD for the two catalyst solubility types: Ni and Cu.

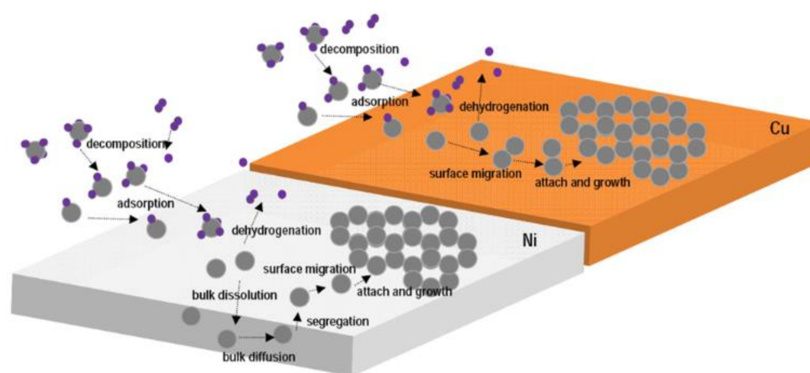

Figure 4: Growth kinetics involved in graphene grown with CVD on two catalyst types with different C solubilities [35].

CVD is a method that shines with its practicality and ease of scalability. Due to its ability to produce large-area good-quality polycrystalline graphene, it is the preferred method for industrial applications such as flexible electronics, solar cells, touch screens and LCDs.

2.2.4 Graphene oxide reduction

Graphene oxide (GO) reduction is another prominent approach to synthesize graphene [36], [37]. In GO reduction, graphene is produced by first, oxidizing graphite to help disperse the graphene sheets, and then, reducing those oxidized graphene sheets to obtain reduced graphene oxide. The oxidation step involves intercalating graphite with an oxidant to introduce functional oxygen groups with the aim of stabilizing and dispersing the graphene sheets in water. A method known as Hummers is the most commonly used to perform this step [38]. In Hummers', a combination of concentrated sulfuric acid and potassium permanganate is employed to disperse the graphene sheets by destroying the sp^2 structure of graphene and forming functional groups such as s hydroxyl (-OH) and carbonyl (C=O) on the basal plane and edges respectively. After oxidation has been carried out, graphite oxide is then separated into individual sheets of graphene oxide through sonication.

Reduction of graphene oxide sheets can be done with three main methods: chemical, thermal, and microwave. The oxidation step has introduced defects into the graphene sheets, and depending on how the reduction step is carried out, some of the defects will be able to be removed. However, at the present time, none of the reduction methods can fully remove all the functional oxygen groups and return graphene to a pristine state [39]. The chemical method involves treatment with reducing agents such as hydrazine hydrate, ascorbic acid, or sodium borohydride among others, to chemically reduce the graphene oxide sheets. The thermal method is carried out by heating up the graphene oxide until the oxygen containing functional groups are decomposed to CO_2 and H_2O. Lastly, microwave reduction is performed by irradiating the graphene sheets with microwaves after oxidation. This causes the sheets to aggressively heat up and decompose into gases like CO_2, CO and H_2O following a very similar process than thermal reduction.

Graphene synthesis via graphene oxide reduction has an immense potential. Low cost and scalability are its main advantages compared to other techniques. However, in its current stage, the graphene generated is far from pristine in quality as none of the reduction methods can fully eliminate the oxygen functional groups. This is so much so, that the graphene obtained through this technique is tagged as reduced graphene oxide (RGO) to clearly acknowledge its defected state. Additionally, further progress is also required when it comes to reducing the waste produced with the technique. Some of the agents used in the Hummers method are toxic and generate a lot of waste, which make this technique environmentally concerning for large scale purposes at present.

In conclusion, graphene synthesis has evolved through various methods, each offering unique advantages and limitations. Mechanical exfoliation provides high-quality graphene but lacks scalability, while techniques like CVD, liquid-phase exfoliation and GO reduction offer scalable routes with precise control over graphene properties but are limited in the quality of the graphene they can produce. In addition to the aforementioned techniques, there are many others such as electrochemical exfoliation and epitaxial growth. Ultimately, the choice of the

graphene synthesis method to use will come down to what technique offers the best combination of advantages and disadvantages for the particular application.

2.3 Material Characterization

2.3.1 Raman spectroscopy

Raman spectroscopy is a pivotal analytical technique that utilizes the inelastic scattering of monochromatic light to investigate vibrational, rotational, and other low-frequency modes in materials. Discovered by Sir C.V. Raman in 1928, this method has become essential in various scientific fields such as chemistry, physics, materials science, and biology due to its ability to provide a molecular fingerprint of substances.

One of the primary advantages of Raman spectroscopy is its non-destructive nature, allowing for the analysis of samples in their native state without extensive preparation. It is applicable to solids, liquids, gases, and biological tissues, and can be performed using fiber optic probes for remote and in situ analysis. This versatility is particularly beneficial in environmental monitoring, forensic science, and biomedical diagnostics.

The principle of Raman spectroscopy involves illuminating a sample with monochromatic light, typically from a laser source. Most photons are elastically scattered, and the exiting light's wavelength is unchanged. This occurs when photons interact with the molecule or solid lattice and their energy is unaltered in a process known Rayleigh scattering. However, a small fraction have their energy changed and undergo inelastic scattering. Depending on the vibrational or rotational energy levels of the molecules, the scattered light can have specific frequency shifts that correspond to those levels. These shifts, known as the Raman effect, provide detailed information about the molecular structure and composition of the sample. When the shift leads to the energy gain of the molecule, that is known as Stokes Raman scattering, and the scattered light's wavelength increases. When the shift leads to the energy decrease of the molecule, that is then called Ant-Stokes Raman scattering, and the scattered light's wavelength decreases. Stokes Raman is statistically more likely to take place, and as such, often more studied over Anti-Stokes in Raman spectroscopy due to the higher intensity of scattered light obtained for the same light-source power.

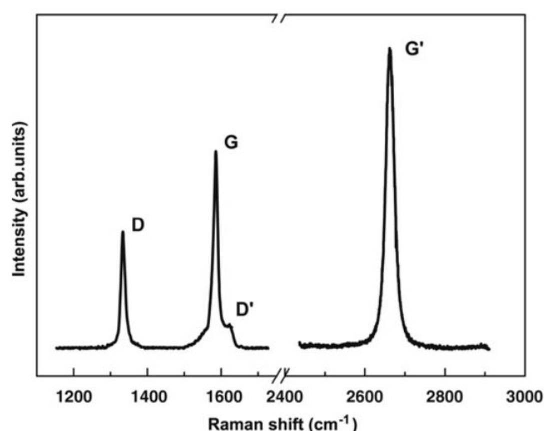

Figure 5: Raman spectrum of a graphene, showing the main features, the D, G and G' peaks taken with a laser excitation energy of 2.41 eV (514 nm) [40]

In the Raman spectrum of graphene, three main distinct bands can be observed (Figure 5): the D band present at around 1350 cm^{-1}, the G band present at around 1582 cm^{-1}, and the 2D band (sometimes also called the G' band) present approximately at 2700 cm^{-1} using laser excitation at 2.41 eV. The D band is associated to the breathing modes of six atom rings and can only be observed in imperfect graphene samples or the edges of pristine graphene sheets. The G band is associated to the high-frequency E_{2g} phonon at the Brillouin zone and can be observed in both imperfect and perfect graphene samples. Lastly, the 2D band is the overtone of the D band and is also associated to the breathing modes of hexagonal atom rings. In this case, however, the 2D band is always present and can be observed in both imperfect and perfect graphene sheets since it originates from a two-phonon scattering process where the two phonons involved have opposite momentum vectors and, as such, momentum conservation is satisfied.

When interpreting Raman spectrums of graphene samples, the characteristics of these bands can be used to extract information about the quality of the graphene, and the number of layers it possesses. In terms of quantifying the defects and disorder, the *I(D)/I(G)* ratio can be used to compare the number of defects between two samples of graphene [41]. As a pristine graphene sample becomes less and less defect free, a D band appears, and the *I(D)/I(G)* ratio increases. As well as the appearance and heightening of the D band, the G band also broadens as graphene is more impure and has smaller grain sizes [41]. In terms of the number of layers, it has been found that the 2D band lineshape and the *I(G)/I(2D)* ratio provide a good indication of the quantity of layers present in the sheet of graphene [41]. SLG presents a 2D band with relatively narrow linewidths (30-40cm^{-1}) and low *I(G)/I(2D)* ratios of 0.5-1. On the other hand, multilayer graphene (3 layers or more) presents thicker linewidths (~70 cm^{-1}) and high *I(G)/I(2D)* ratios of 1.5-3.

2.3.2 Scanning electron microscope (SEM)

Scanning Electron Microscopy (SEM) is a fundamental imaging technique that plays a crucial role in various scientific and industrial fields. SEM is widely used for investigating the surface morphology, microstructure, and composition of materials at a high resolution, making it indispensable in material science, biology, nanotechnology, and electronics.

The basic principle of SEM involves scanning a finely focused beam of electrons across a sample's surface. As the electron beam interacts with the sample, it generates different signals, including secondary electrons, backscattered electrons. These signals are detected and used to create detailed images of the sample's surface.

The process starts by electrons being accelerated and launched against the sample. Once they reach the sample, they defuse into it, generating a bulb-like shape known as the interaction volume. The size and depth of this shape depends mainly on the density of the specimen observed as well as the electron energy. Diffused electrons can then scatter elastically or inelastically depending on the interaction with local atoms. When inelastic scattering takes place, secondary electrons are generated. These electrons are produced from the emission of valence electrons from the atoms of the sample. Secondary electrons are the primary type of electrons generated and are particularly valuable for producing high-resolution images that reveal fine details of surface topography. Only surface information can be obtained because

secondary electrons have very little energy associated to them and the ones produced inside the volume are quickly absorbed by the specimen.

On the other hand, when elastic scattering takes place, backscattered electrons are generated. Backscattered electrons are high-energy and, as such, are able to provide deep region information as well as specimen composition.

As illustrated in Figure 6, a scanning electron microscope (SEM) consists of several key components that work together to produce high-resolution images of a specimen's surface. The electron gun is the source of a focused beam of high-energy electrons, which is typically generated through thermionic or field emission. Electromagnetic lenses, including condenser and objective lenses, focus and control this electron beam, directing it precisely onto the sample. The scanning system, made from scanning coils, deflects the focused beam across the sample's surface in a systematic raster pattern, enabling detailed imaging. The specimen is housed in a vacuum chamber to prevent interference from air molecules and ensure beam stability. Detectors, such as secondary electron and backscattered electron detectors, capture electrons emitted from the sample, forming detailed images and providing compositional contrast. Finally, the display and control system process the detected signals and presents them as images for analysis, offering insights into the sample's surface structure.

SEM is an indispensable tool in the realization of this work. This imaging technique is used for the top-view and cross-section evaluation of all anodized samples. It is also used to inspect the plasma etching results where alumina is used as a mask. A Hitachi Regulus 8230 is used with an acceleration voltage of 1kV.

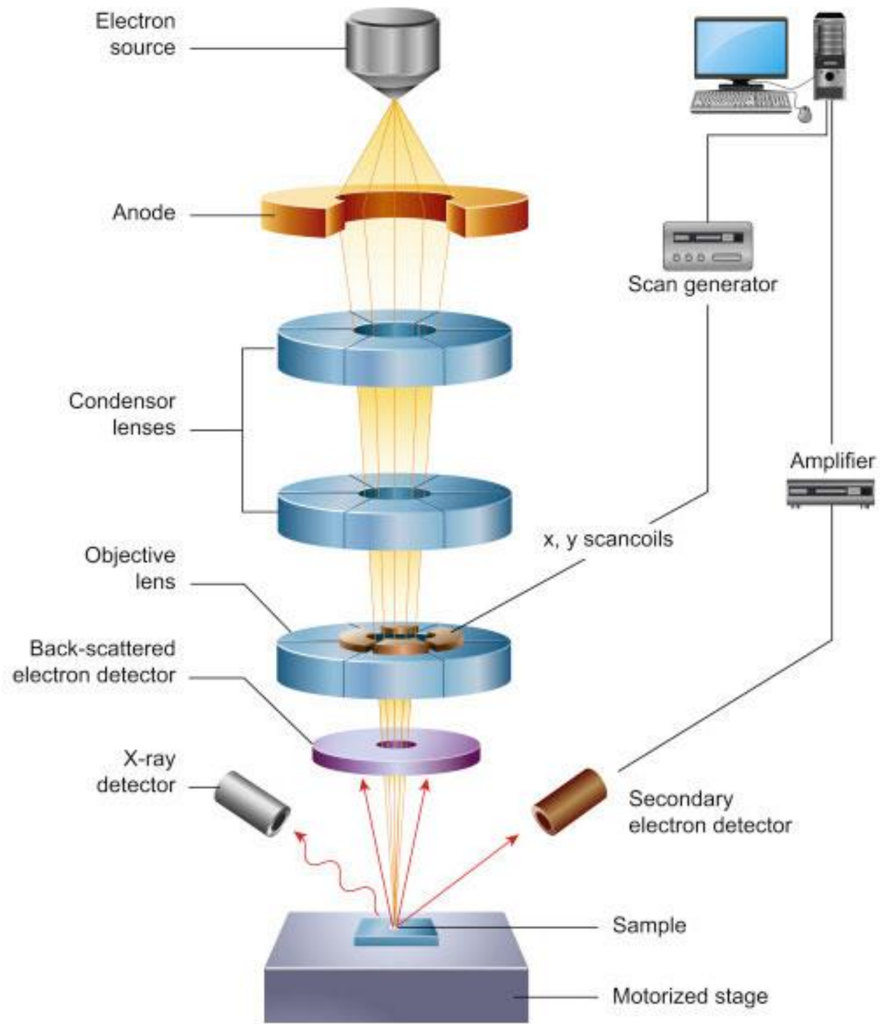

Figure 6: Schematic of a scanning electron microscope.

3 EXPERIMENTAL METHODOLOGY

In the experimental methodology section, the full experimental process realized in this work is described. The section is divided into three main parts. In the first part, the graphene growth technique used in this thesis is explained in detail. The second part focuses on the anodization process. The setup used, including the custom 3D printed pieces and the instrumentation needed, is showcased together with all the specific steps and parameters required to obtain the alumina mask. Lastly, the third part explores the plasma etching method used to pattern the graphene using that alumina mask.

Before the main contents of this section, a small subsection describes in a broad manner the entire step by step flowchart followed in this thesis to pattern graphene with a hard alumina mask to obtain graphene nanomesh.

3.1 Full process flowchart

The process begins with a single-side polished, 500µm thick, 4-inch silicon wafer. Firstly, 600 nm of SiO_2 are grown on top using wet oxidation Figure 7a). This is done to insulate and protect the bulk of Si and also to prevent Mo from diffusing into it. Then, a thin layer of 50nm of Mo is deposited on top using sputtering Figure 7b). This layer acts as the transition metal catalyst for the growth of graphene by CVD. The layer is then patterned in a photolithographic process. 3.5 µm of Nlof2020 negative photoresist are deposited and soft baked on top of the wafer Figure 7c). The photoresist is subsequently exposed using ASML PAS 5500/80 and a 10x10mm open mask in a 20mm die size. The wafer is developed right after Figure 7d), and the Mo is dry etched using an SF_6 based recipe in the Trikon Omega 201 Figure 7e). The remaining resist is removed in the Tepla stripper with 10 minutes of oxygen plasma Figure 7f).

After Mo has been patterned, the graphene growth process by CVD takes place Figure 7g). This synthesizes a layer of graphene only on the surface of patterned Mo squares. Once the process is over, pure Al is sputtered on top of the entire wafer Figure 7h). The wafers are then diced into 20mm die size samples.

These samples are then taken to the anodization set up and anodized Figure 7i). The previously deposited Al layer transforms into a thinner layer of nanoporous alumina on the center part of the samples where the square of graphene is located. In the final step of the process, the samples are dry etched using a plasma recipe with O_2 and SF_6. The nanoporous alumina acts as a hard mask and the graphene layer is etched only on the areas that reside below the pores. Graphene nanomesh is formed. The schematic of the entire fabrication processes is illustrated in Figure 7.

It is important to note that, in the beginning, it was attempted to skip the patterning step and grow graphene in the entire surface of the wafer. However, the adhesion of the Al layer that was sputtered on top afterwards was remarkably poor, and the metal layer would detach while attempting dicing. It is for that reason that the idea of patterning the Mo was thought of. If graphene is only grown on the center 10 by 10 mm area of the 20 by 20 mm dies, the cutting process, which is most aggressive on the edges of the cut, engages exclusively with Al sputtered on top of SiO_2. This is known to not cause issues as the adhesion between the two is really

good. It was also attempted to sputter Al on the dies after dicing as an alternative. However, the poor adhesion between the layers caused the samples to fail and delaminate during handling in the anodization step.

As well as wafers with Al deposited on top of graphene, wafers with only Al deposited directly on the Si were prepared. These wafers were used as optimization samples, to test the setup and the full anodization process, so that the results could be fine tuned without wasting many wafers with graphene. Several Al thicknesses were tested as it will be explained in more detail below.

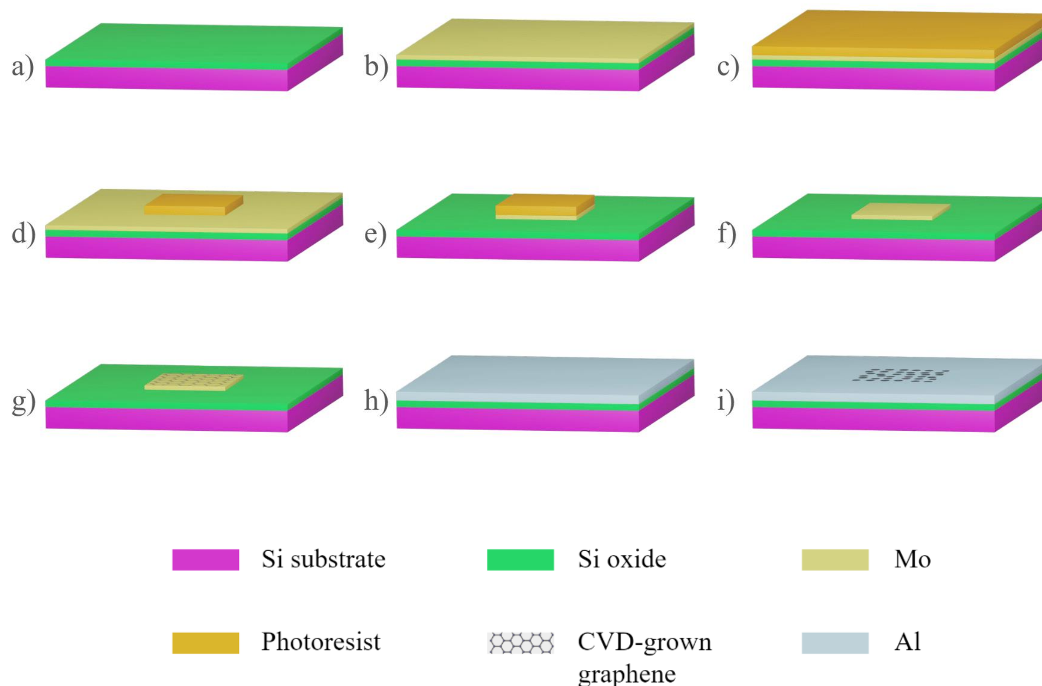

Figure 7: Schematic of the complete wafer process flowchart.

3.2 Grapehene growth

In the present work, the method of CVD is chosen to synthesize graphene. This technique was selected for its capability to produce wafer-scale graphene layers with relatively good quality. Despite this method not being able to produce monocrystalline single-layered graphene sheet, the multilayered polycrystalline sheet with micrometer-sized domains that can be achieved with this technique suffices for the purposes of this work.

The process begins by sputtering a thin layer of 50nm of Mo on the surface of 600nm of SiO_2, which was grown using wet oxidation. Mo is the transition metal chosen for the CVD process due to its high melting point of 2623ºC. This allows the catalyst layer to be very thin with no risk of segregation at the high temperatures required during the CVD. Additionally, this enables the Mo layer to be pre-patterned selectively if needed.

After that, graphene is deposited on the Mo catalyst using a commercially available AIXTRON BlackMagic Pro at 935 °C. The process comprises of 20 minutes of pre-annealing of the catalyst to remove any surface oxides and 20 minutes of growth. CH_4 is used as feedstock.

3.3 Anodization

3.3.1 Anodization Setup

3.3.1.1 Custom anodization cell design

Experimental setups used to study aluminium anodization and porous alumina layers, traditionally use a solid block of aluminium submerged in the electrolyte bath as the cathode. This simple approach of using a block of aluminium as the electrode is usually sufficient to study nanoporous alumina. Aluminium is exclusively reacting with the electrolyte and the reaction can be monitored properly. In this work, however, aluminium is to be anodized on top of graphene, and as such, the fabricated samples have exposed graphene and molybdenum on the sides once they have been diced. Submerging a diced wafer with exposed material other than aluminium would pose a risk for having an uneven anodization reaction rate, as other reactions could take place on the sides in addition to anodization. Having even reaction rates is fundamental to controlling the pore formation mechanism and obtaining precise alumina thicknesses. It is for this reason, that a custom-made anodization cell was made for the realization of this thesis.

The anodization reaction takes place inside a beaker with the electrolyte solution. The task of designing custom pieces to perform aluminium anodization under the conditions of this work, is devided in 3 main parts. Firstly, designing a holder for the cathode. In the anodization of aluminium, the work of the cathode is only to be conductive and not participate in a chemical reaction with the electrolyte. The two most used inert electrodes that would fit those characteristics for our electrolyte are platinium based electrodes and graphite based electrodes. Graphite was chosen as the material to use for the cathode in this case as it is much more cost-effective than platinum. Therefore, the first task was the design of a piece to support a graphite electrode.

The second part involves the design of a holder for the anode. The anode is the electrode where oxidation takes place. For this work, that corresponds to the wafer piece with graphene and aluminium deposited on top.

Finally, the third part is the design of a main support piece that holds the two previous pieces together at a particular orientation and distance from each other. It also fixes them at a particular position in the electrolyte bath by gripping the beaker where the anodization takes place. This is important as the direction of electric field generated in relation to the surface of the aluminium determines the direction of growth of the pores. Lateral-PAA templates can be formed when cathode and anode are positioned perpendicular [42]. For the purposes of this thesis, however, the pores must be grown vertically. As such, the two pieces will be held in front of each other in a parallel orientation.

Due to the relatively small size, and the low mechanical requirements, 3D printing was chosen as the technique to use for the fabrication of the pieces. This method of additive manufacturing

is a great choice due to its low cost for low production numbers and its ability to produce almost any custom shape with very few design constrains (depending on the specific type of printing technique used). As the most common electrolyte solutions used for nanoporous anodic alumina are phosphoric acid, sulfuric acid, and oxalic acid solutions, a polymer was chosen to be able to endure any of those solutions without swelling or breaking down. Polypropylene (PP) was the final choice for the material, not only for its excellent chemically resistant properties (which allow any of the aforementioned electrolyte options), but also due to the popularity of the material in the desktop 3D printing space and how available it is for that reason in many different printing techniques.

Anode holder

The main requirements for the design and construction of this anodization cell are the following. Firstly, the anode cell needs to be fully watertight and only expose aluminium to the electrolyte. The surface of aluminium exposed should be ideally as large as possible to facilitate a more even anodization process. Additionally, the larger the surface anodized, the higher the current signal will be for a given potential. Higher currents will produce less noisy readings of the current-time curves when the reaction takes place.

Secondly, there needs to be direct electrical connection to the surface of the aluminium. The positive electrode of the power supply must be connected to the aluminium so that the metal can act as the anode in the electrolytic cell reaction. This connection has to be made from the front of the sample where the aluminium sits. The silicon oxide layer would otherwise prevent the flow of current.

Finally, the piece that holds the aluminium needs to have a simple opening and closing mechanism that does not break watertightness and is not destructive. To be able to experiment with the different anodization parameters and fine tune the process, many anodizations tests need to be performed. For this reason, it is essential that the anodization cell is designed with a simple loading system for the cathode piece so that many samples can be anodized without requiring complex steps or constant replacement of parts.

First design: o-ring seal with foam backplate

A first design was done using o-rings as the sealing mechanism. The design features two o-rings: a big outer one and a smaller inner one. The small o-ring has a size of 12mm of internal diameter and 2 mm of cross-sectional thickness. Its purpose is to expose the aluminium to the electrolyte bath through the area in the center while providing a water-tight seal that prevents the solution from touching anything else or entering the anode piece. This small o-ring is placed on a circular chamber located at the end of an arm-like shape that altogether forms the solid main piece of the anode design. The circular chamber is where the samples are loaded, and it has a circular opening in the center where the sample is placed and where anodization takes place. The arm-like shape is responsible of carrying electrical connection from the top of the beaker, to its center, below the water level of the electrolyte. It is a solid piece of material with a void channel inside that allows for a cable to be routed through and not get wet. This channel is connected directly to the chamber, and electrical connection between the cable and the front-side of the sample is made through the use of micro springs (to which the cable is connected

to). The springs lay upright on the inside surface of the chamber, parallel to the main opening and are placed very close to it. They are 8 mm in height, and they surpass by less than 2 mm the height of the opening of the chamber on the inside. That way, when a sample is loaded and reaches the o-ring, the springs are very so slightly compressed and make good contact with the surface of the aluminium.

The big o-ring has a size of 60mm of internal diameter and 2.5 mm of thickness. It is placed on the outer wall of the chamber of the main piece, and its purpose is to make a water-tight seal with a backplate, so that the chamber can be opened and closed for the loading and unloading of samples. The backplate is a secondary smaller piece, with the same shape as the circular chamber but much flatter. As well as its purpose as a lid, the backplate also functions as the element that provides backpressure to the sample so that a seal can occur between this and the inner o-ring. In this first design, this backpressure is provided by a small pillar of 5 mm thick EPDM foam. The seal between the backplate and the main chamber piece is held together by 4 PP 8 mm cs screws that press the two pieces against each other and the o-ring. These screws are spread around the outer part of this clamp mechanism.

Both o-rings were purchased in EPDM rubber, with the lowest hardness level available for that material and size (shore A 70). EPDM rubber was selected as the material of choice for the o-rings as it is a very available material for o-rings that is relatively inexpensive, and has great chemical compatibility properties compared to the other common polymers used such as silicon and nitrile (which catastrophically swell when exposed to phosphoric acid at high concentration or temperature). The hardness was selected to be the lowest possible, as the function of the o-rings in this work requires them to hold very little pressure, and increasing softness makes achieving a perfect seal an easier task for the same backpressure.

The pieces were printed in PLA first, on an Ultimaker 2 desktop FDM 3D printer to test the o-ring fit and the watertight capabilities of the design. After a successful test, the pieces were then sent to be professionally printed in PP by multi jet fusion (MJF) printing. This method of printing was chosen due to its low cost compared to other printing techniques, and its high resolution (Higher than FDM as it prints layer by layer with 0.1mm of resolution limit on the Z axis).

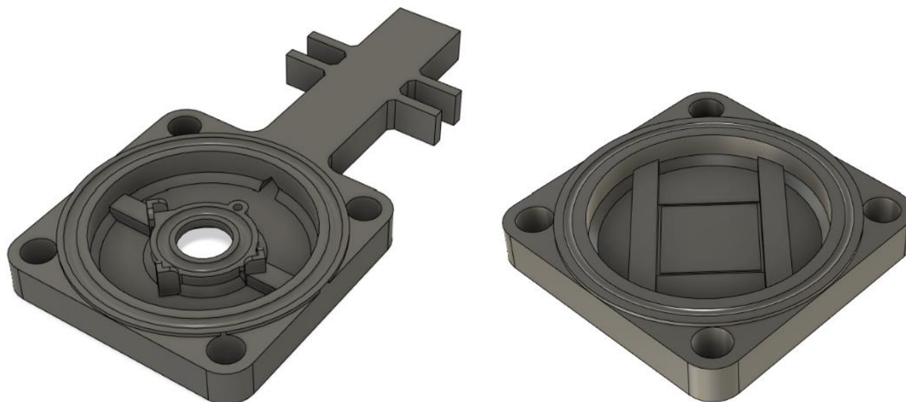

Figure 8: 3D model of the first anode support design. The main chamber piece can be seen on the right, and the backplate on the left.

Unfortunately, after the final piece was fabricated and delivered, it was found to leak. The cell was able to perform short anodizations, but after being submerged for more than 20 or 30 min, the chamber would slowly fill up with electrolyte. This failure was attempted to be fixed by changing the o-rings multiple times, and adding more foam on the backplate to increase the sample backpreassure. However, none of this fixes managed to solve the problem. As depending on the samples are anodization parameters, the possibility of performing long anodizations was a requirement, the decision was made to redesign the model.

Second design: softer o-ring seal with spring backplate

The second design follows the same design characteristics as the first one. The sealing method are two o-rings: one responsible of exposing the electrolyte to the sample, and another one responsible to make a watertight seal with a backplate, allowing the chamber to be opened and closed to load and unload said samples. The main difference with the previous design, are the size and softness of the o-rings. For this iteration of the anode piece, thicker and softer o-rings were purchased.

The previous design had failed at the o-ring/PP interface, where the water slowly leaked through due to the high porosity of the PP surface. A softer and thicker EPDM rubber would be able to conform to that porosity better and prevent any electrolyte from getting into the chamber. As shore A 60 EPDM (the next level of softer o-rings) have very limited availability, two o-ring were bought with ID sizes bigger than in that of the original design. A big one with 70mm in ID and 3.5mm in CS thickness, and a smaller one with 16mm in ID and 3mm in CS thickness. These dimensions, although just ever so slightly larger, had compatibility issues with the beaker and sample size. The big 70mm o-ring would cause the new chamber to not fit inside the double walled beaker, and the small 16mm o-ring would get so close to the edges of the sample, that it would make the alignment of sample with the inner o-ring problematic with a very small room for error.

To solve these problems, two changes the design of the chamber were made. Firstly, the outer shape of the chamber was changed from a circle to a vertically oriented oval. In doing so, the outer o-ring could be fitted in the chamber also with that vertical oval shape, and the horizontal footprint of the chamber was equal in size to the previous design, allowing the main piece to fit inside the beaker. Secondly, the inner o-ring was fitted in the chamber with the shape of a square with big bevels. That shape instead of the circular one, allowed for bigger tolerances in the alignment of the square sample and the previously circular now also square inner o-ring.

The other significant difference with the first design is the backplate system. The previous iteration featured EPDM foam as the system to apply pressure behind the sample to create a seal between its surface and the o-ring. While this provided an adequate level of pressure, the amount it produced decreased as several anodizations were performed and the foam slowly collapsed. To guarantee even pressure throughout multiple anodizations and increase the lifespan of the backplate mechanism, two small compressive springs of 5mm of diameter and 10mm in length were used instead.

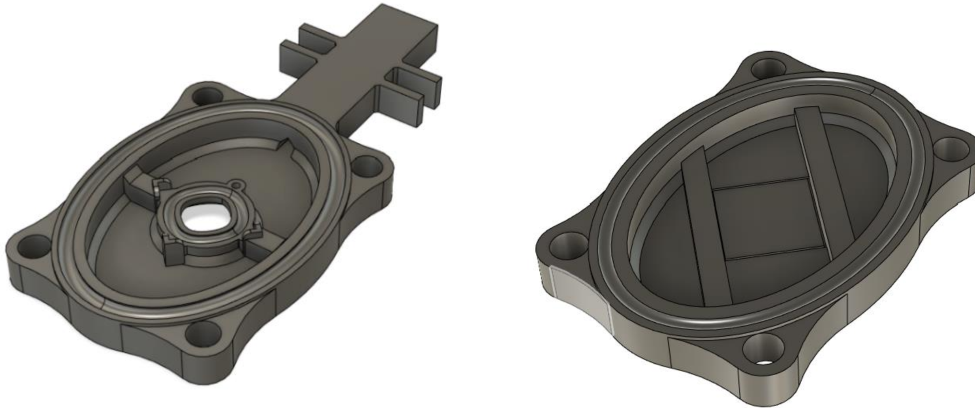

Figure 9: 3D model of the second anode support design. The main chamber piece can be seen on the right, and the backplate on the left

Despite these changes, the anode piece was found to leak once again. No matter how hard the outer screws would be tightened, water managed to penetrate the piece and flood the chamber in about 30 minutes. The extra softness and thickness of the o-rings did not manage to overcome the roughness of the surface of the MJF 3D printed PP pieces, which was likely the cause of the leaking issues. A new anode cell piece had to be designed.

It is important to mention that for both this second design and the first one, a prototype was made by printing the piece in FDM PLA first, to test for watertightness. However, due to the smooth finish of the extruded plastic for FDM printing, the seal worked successfully in both tests and failed to offer an authentic representation of how the final material would behave. This made the iterating process really challenging as any change in the design could only be tested by sending the file to be professionally printed, investing a considerable amount of money and time.

Third design: EPDM foam seals with foam backplate

The third design followed the same concept of the two previous designs, having a main chamber piece and backplate piece, and an outer and inner seal. In this case, however, o-rings as the sealing mechanism were discarded and replaced by foam instead.

EPDM foam sheets with thicknesses as high as 5mm and more can be easily and cheaply purchased online for multipurpose insulation. These foam sheets are extremely malleable and soft. The 5 mm of thickness offers a significant headroom for the material to deform and effortlessly conform to rough surfaces. While being a poor choice for high water pressure applications [43], this soft foam is the perfect sealing mechanism for this application where the chamber is submerged a few cm under water level.

For this piece, a sheet of 5mm thick EPDM foam was used as the inner and outer seal. As the foam can be cut into any shape, and the sample is a 22x22 mm square, the seals were cut into rectangular shapes. This minimizes the size of the chamber and backplate pieces needed for the same area of even width seal. This also applies to the inner seal with the sample.

For electrical connection, the method of having micro copper compressive springs was replaced for a different approach. The copper springs required small cylindrical supports on the inside of the chamber that increased the thickness by almost 10mm for the entire main piece. Additionally, their availability was very limited and every time the chamber got flooded, they would have to be replaced as the electrolyte would oxidize the copper. Furthermore, the set-up process was elaborated as the cable had to be routed through all 4 springs and the chamber was too small to allow for easy manoeuvrability.

In this new design, copper tape was used instead. Thanks to the softness of the foam, a bit of copper tape could be adhered to the inner foam seal without breaking watertightness. That same tape extended to the end of the arm section of the main piece acting as a cable. Connection was established with the positive end of the power supply by means of alligator clips.

For the backplate pillar, EPDM foam was used again on top of a 3D printed PLA extension. EPDM foam was used as in this design, the sealing mechanism is also made out of foam, and has a large, compressed depth margin to achieve a good seal compared to the o-rings which are relatively very rigid.

This final design met all the set requirements. Anodization processes longer than 5 hours were performed without any leaking issues. The realization of this thesis work in its entirety was done using this cell piece.

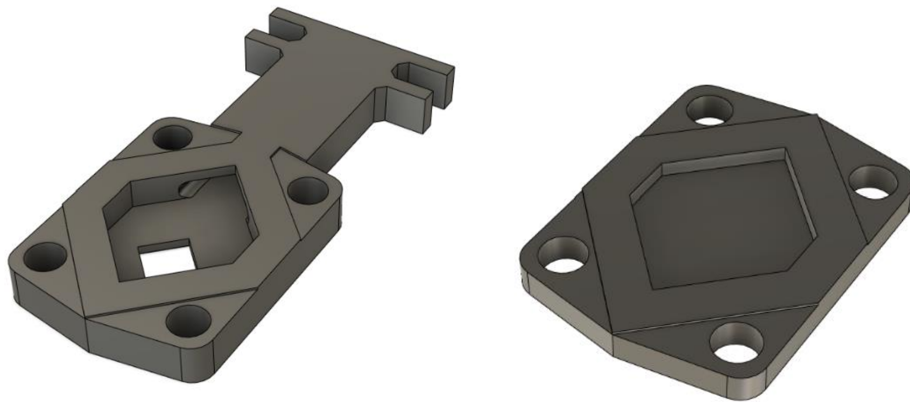

Figure 10: 3D model of the third anode support design. The main chamber piece can be seen on the right, and the backplate on the left

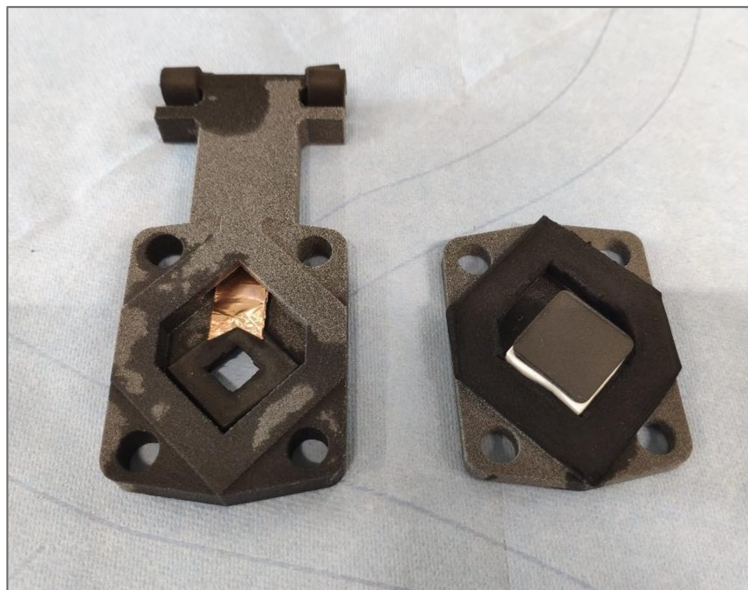

Figure 11: Printed pieces of the third and final anode support design

Cathode holder

The cathode holder follows a much simpler design compared to the anode holder. Two brackets of equal dimensions clasp a graphite block in the middle through the use of PP 6mm cs screws. These bracket pieces have a horizontal gap that extends wider than the graphite block, allowing them to grab onto the slot of the main support piece (as it will be explained in more detail in the following section).

The graphite block, of 100x50x5 mm dimensions, is grabbed on the upper part and extends into the electrolyte bath for more than half its length. The brackets have a small rectangular opening that runs from the top to the centre and allows for part of the graphite block to be exposed on its upper part. This opening provides space for alligator clips to bite into the block directly and make easy electrical contact.

Main support

The main support piece holds both holders together and attaches them to a beaker in their appropriate places. The piece has a disk-like shape with a diameter slightly larger than that of the beaker. A 50mm wide slot runs along its center and extends from one end to the other. Both holder pieces fit in with the main support piece using this slot. Horizontal openings of the same profile than the cross-section of the slot allow the pieces to be attached and held together in the centerline of the structure.

Thanks to this rail-like design, the distance between the holders can be easily adjusted. This is an important feature as that parameter could require tinkering to optimize self-ordered pore formation. To easily control how separated both electrodes are, the main support piece has distance marks with mm precision that run parallel to the slot.

The disk grabs on to the top of the beaker with a protruding lip. This lip has a diameter slightly larger than that of the beaker. With the help of some EPDM foam adhered to the inside of the lip, a snug pressure fit is achieved between the two elements.

Figure 12: Image of the three 3D printed supports mounted together. The cathode support can be seen with a block of graphite on the left. The main support can be seen on top holding the two other supports together.

3.3.1.2 Laboratory instrumentation

To perform the anodization of samples, several instruments take part in setting the conditions and monitoring the different parameters.

Firstly, the anodization takes place inside of a double walled beaker of 10 cm of inside diameter. The beaker is connected to a chiller (Huber K6-mpc-NR) in a closed loop that runs a mixture of water and ethylene glycol through the inside of the double wall. This allows the temperature of the electrolyte to be set at a stable value.

The beaker is placed on top of a magnetic stirrer with hot plate and temperature control functionality. This stirrer serves two purposes. On one hand, it provides vigorous stirring with the help of a 2cm magnetic stirrer bar that sits at the bottom of the beaker. Stirring is essential in nanoporous aluminium anodization to prevent bubble formation that can perturb the pore formation process. On the other hand, the stirrer monitors the accurate temperature of the electrolyte solution with the aid of a digital thermometer with a glass cover. Despite the cooler having accurate temperature control of the cooling solution, the beaker is not thermally isolated from the outside environment, and as such, the electrolyte does not match the temperature of the cooling loop and sits at a few degrees Celsius higher. The thermometer is placed inside the solution from the top and is supported by a lab stand with a clip attachment.

A commercially available SM120-25D Delta electronika power supply is used to provide power. 18 AWG test leads with alligator clips connect the positive and negative ends of the supply to the graphite block and the copper tape of the cathode and anode holders. The proprietary software Delta electronica on a desktop pc allows for the monitoring and recording of the anodization signals. The connection is done via an ethernet cable that establishes a local area network.

Lastly, all reactions take place under a fumehood. Some of the electrolyte and solutions that can be used, especially sulfuric and phosphoric acid, can release harmful fumes depending on the concentration and temperature used.

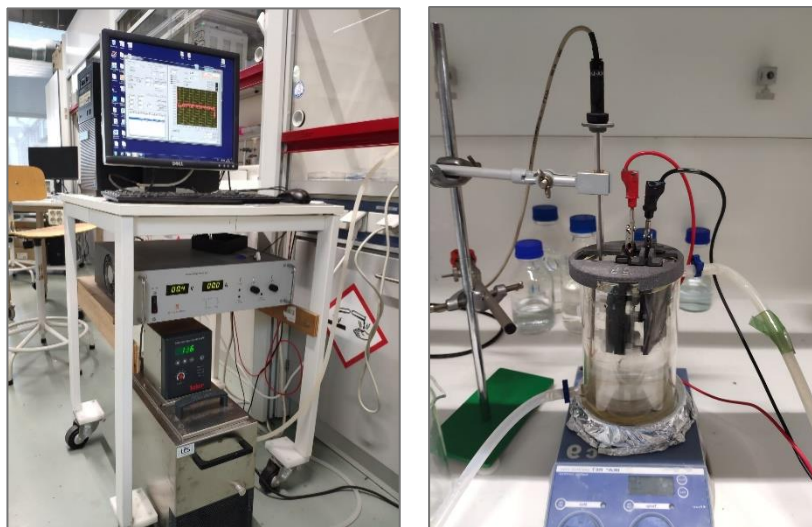

Figure 13: (a) Computer, power supply and chiller used, at the top, middle and bottom of the image, respectively. (b) Image of the beaker used for anodization, with the 3D printed cell inside, the magnetic stirrer underneath, and the digital thermometer used to track the temperature.

3.3.2 Anodization conditions

The anodizations performed during the realization of this thesis were done under the following anodization conditions.

Oxalic acid was used for the electrolyte composition. This acid was chosen mainly for its ideal pore morphology dimensions. The optimum parameters found by Masuda et. al. [18] for this electrolyte are 40V of potential with 0.3M of concentration, which produces pore sizes of 30 to 40 nm approximately (as potential and pore diameter share a direct linear relationship). If sulfuric acid were chosen instead, the optimum parameters would yield 20 to 25 nm pores. It is important for pore size to not be too small, as the smaller the pore size is, the larger the aspect ratio of the pores would be for a given alumina thickness, and the harder it would be to use as a mask in a plasma etching process. Smaller pores could be experimented with in the future, but for the purposes of this work, oxalic acid is a better option to prove the viability of the alumina oxide as a transfer-free mask. Phosphoric acid would have also been a good choice in this regard, and perhaps even a better one since its optimum self-ordering potential is 195V, which yields pores of 150 to 200 nm. However, at the time of making this thesis, there were no

available power sources on site that could reach such a high voltage. Therefore, for all these reasons, the electrolyte composition chosen to perform anodization is 0.3M Oxalic acid with 40V of anodization potential.

The temperature of the electrolyte bath was set at 15ºC. The higher the temperature at which the anodization takes place, the higher the current density is, and the faster the reaction goes as a result. Having faster alumina growth speeds is beneficial, as it reduces the time it takes to anodize a sample for a same given thickness. However, temperature can not be too high. If the temperature of the electrolyte is too high, bubbles can form on the surface of the sample, endangering the quality of the alumina layer. 15ºC is a good balance point between these two factors that has been shown to work in the past with the chosen electrolyte composition and potential [23].

Anodization experiments took place in 700ml of volume of electrolyte. This volume is close to the maximum capacity of the double walled beaker used in this work. Having a large electrolyte reservoir is beneficial as the solution is then less susceptible to sudden abrupt temperature changes due to its higher heatsink capacity. Additionally, a large electrolyte volume increases the longevity of the bath as the acid concentration decrease becomes less significant for the same amount of acid used and depleted. A detailed explanation of how the electrolyte is maintained to guarantee constant conditions is described in the next section.

Stirring was kept constant for all tests at 650 rpms. It has been shown that stirring intensity directly influences the temperature of the sample [23]. Setting the magnetic stirrer to a different rpm would decrease the cooling the electrolyte causes on the sample, which would equate to anodizing at a different electrolyte temperature, altering the current density and the pore growth process.

3.3.3 Electrolyte maintenance

To make sure the integrity of the electrolyte bath was always in proper conditions to perform anodization, several things were done. To verify the levels of oxalic acid had not decreased excessively to the point of altering significantly the speed and characteristics of the self ordering pore formation process, the pH level of the electrolyte was measured every few samples anodized with a digital pH meter that was calibrated before each measurement. The first time, 5 pH measurements of the newly prepared 0.3M Oxalic acid electrolyte solution were performed and a mean value of 1.2 was obtained. After that, measurements would be made periodically and compared to the original measured value plus minus two times the standard deviation. If the pH levels measured exceeded that range, the solution would be replaced.

Additionally, the bath was filtered regularly with filter paper and a glass funnel. This was done to remove particles present in the beaker after extensive use.

Lastly, after every month of use approximately, the electrolyte solution was replaced in its entirety regardless of its particle or pH condition.

3.3.4 Anodization tests – Establishing anodization speed

Before performing the Masuda et al. two step process, single step anodizations are done to stablish the anodization speed for the chosen conditions. This speed is used later to calculate the amount of anodization time needed for the first anodization step of the two-step technique to end up with a thin alumina layer of the desired thickness. Four practice samples of 5 µm of Al on top of Si are anodized in 0.3M Oxalic acid at 40V and 15ºC during different times: 40, 30, 20 and 10 minutes.

After anodization, these samples are cut in half with a diamond tip engraver, and their cross-section is observed with an SEM. For each sample, the cross-section of each layer, alumina and aluminium, is measured 6 times in different areas as shown in Figure 14. Figure 15 is the plot of the measured thicknesses, where the formation speeds for the different layers can be observed.

As it can be seen, the standard deviation for the measurements of oxide is considerably smaller compared to the aluminium measurements. The measurements of the aluminium layer thickness are not as reliable due to the softness and ductility of the material, which cause layer deformation on the cross-section when the die is cut. Another important thing to note is that the oxide formation speed is higher than the anodization speed of aluminium. That means the ratio of oxide formed per aluminium anodized is higher than one.

Since remaining aluminium measurements are not as reliable as the oxide grown ones, to accurately calculate the ratio, a sample is anodized for more than 80min to guarantee all aluminium has been anodized. Then the alumina layer is measured, and the value obtained of 8µm is divided by the reliable known initial aluminium thickness of 5µm. Under the anodization conditions of this work, the ratio is found to have a value of approximately 1.6. Now, this ratio is used on the obtained oxide growth speed, to calculate a more accurate anodization speed.

The aluminium anodization speed for the anodization conditions used in this work is 59.7nm/min. This is the value used when designing all two-step anodization tests to calculate the required anodization times needed to obtain the desired final mask thicknesses.

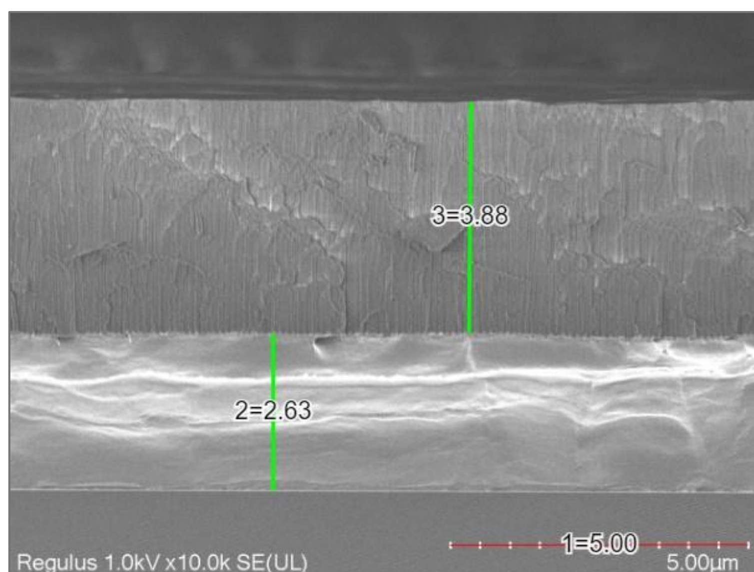

Figure 14: Example of cross-section SEM image being measured. The image belongs to a 40min anodization sample.

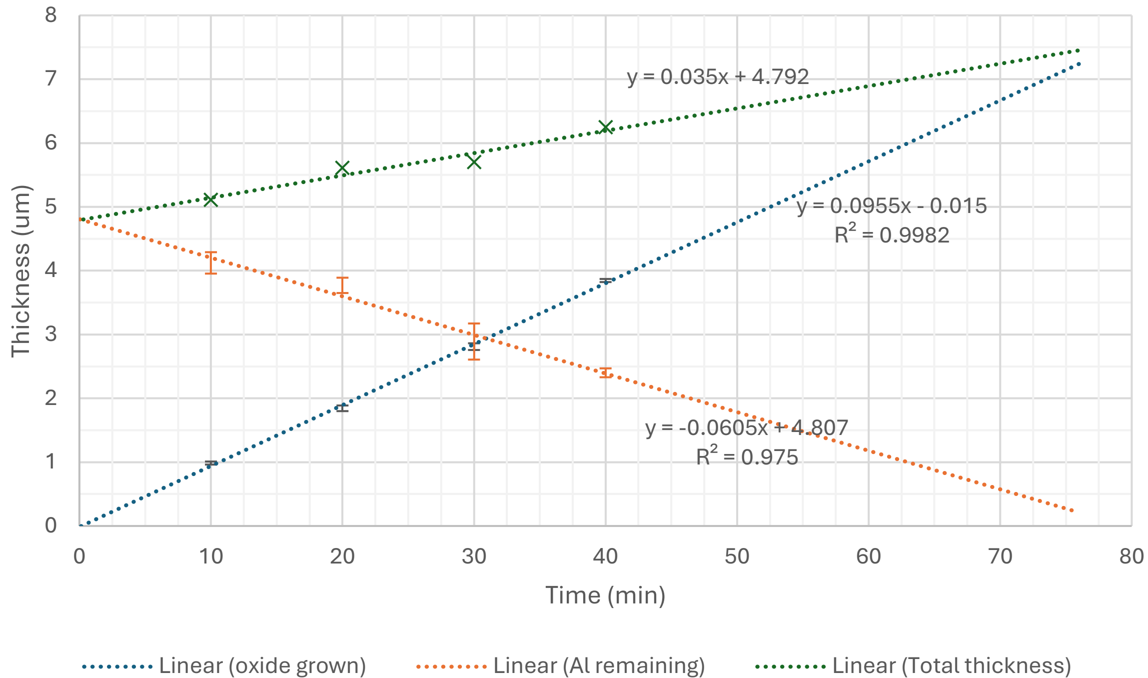

Figure 15: Measured alumina and aluminium layer thicknesses of Al-on-Si samples anodized for different times. Thickness of aluminium remaining: orange marks; Thickness of oxide grown: blue marks; Total thickness: green marks; Linear trend lines: dotted lines.

3.3.5 Anodization tests - Stripping process

Once pore growth has been observed and the anodization speed has been established for the chosen anodization conditions, the effectiveness of the stripping process is tested. This process is the last step of the two-step process to be tested individually.

The stripping process in the two-step technique has been commonly done by introducing the sample in a hot bath of a mix of 0.4M H_3PO_4 and 0.2M H_2CrO_4 at 60ºC for a certain amount of time [18]. This time can range from 5 minutes, to as long as 14 hours in some cases. The time needed to fully dissolve the alumina layer depends on the thickness anodized in the first step. However, under regular conditions, it is acceptable to leave the sample in the bath for more time than needed. Samples can be stripped overtime to guarantee complete alumina removal.

The acids that constitute the stripping solution serve two different purposes. Firstly, the 0.4M H_3PO_4 serves the main purposes of the stripping solution, which is to dissolve the alumina layer. Secondly, the 0.2M H_2CrO_4 is used to prevent corrosion on the remaining Al surface, once the alumina on top has been stripped. It has been demonstrated [44] using the weight loss method and inhibition efficiency (η), that as corrosion inhibitor for aluminium in 1.0 M H_3PO_4 at 30ºC, potassium chromate (Cr(IV) compound) is highly effective as it prevents corrosion with 99% efficiency η. However, chromate is recognized as both highly toxic and carcinogenic. Due to its high hazardous classification, its use was unfortunately not allowed for the realization of this work.

A recent study focused on finding alternative "green" inhibitors, studied the corrosion inhibition properties of the molybdate ion (MoO_4^{2-}) [45]. It was found that this ion acts as a good inhibitor

on aluminium in 1.0 M H_3PO_4, achieving a maximum corrosion efficiency η of 91.2% with 20mM of Na_2MoO_4.

In this work, a solution mix of 0.4M H_3PO_4 and 0.1M of Na_2MoO_4 at 60ºC is used as the stripping solution to remove alumina. The concentration of 0.1M of Na_2MoO_4 is chosen instead of 20mM. This is done because the concentration of H_2CrO_4 that is traditionally used in two step processes is also several times higher (0.2 M) than the concentration found needed to inhibit corrosion in aluminium in 1.0 M H_3PO_4 at 30ºC (0.005 M).

To test the effectiveness of the new solution, a stripping process test is performed. A 5 µm aluminium sample is anodized in 0.3M Oxalic acid at 40V and 15ºC for 40 minutes. This layer is then removed by submerging the sample in 400ml of 0.4M H_3PO_4 and 0.1M of Na_2MoO_4 solution at 60ºC during 15 min while stirring. The sample is then cut in half using a diamond pen and its cross-section is observed with an SEM.

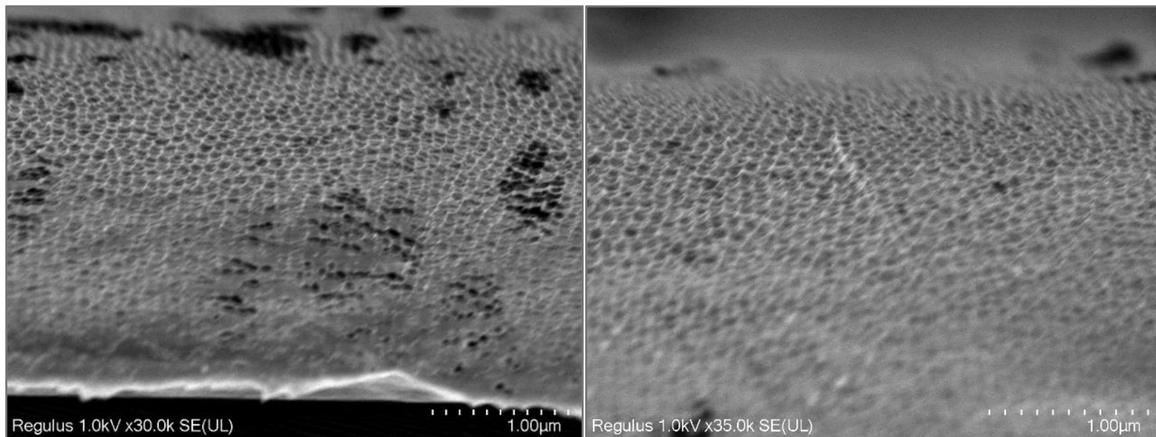

Figure 16: Cross-section SEM images of aluminium surface after anodization and stripping test.

Figure 16 shows the cross-section of the sample at its top-side surface. Despite the sample being observed at its cross-section, part of the top-side surface can be observed in the images. This is because these images were taken at a delaminated section that was hanging from the main piece with a slight angle. The choice was made to photograph the sample in this spot as here the surface topology can be observed with more clarity.

As it can be seen, after performing the stripping process, the sample is left textured with an array of dimples that cover the entire surface. This array of dimples is the expected surface topography for the aluminium after performing self-organized alumina pore growth. The dimples are the result of the mechanism in which the pores grow at the aluminium/oxide interface during anodization. When the alumina is dissolved after anodization, the imprint of the bottom end on the pores is left on the aluminium and it can be observed on the surface as dimples. These dimples are crucial in the Masuda et al. two step process as they provide a fixed starting point for new pores were a second anodization step be performed, allowing pore ordering conservation.

It is important to note, that another test was done with a stripping solution with 0.2M of Na_2MoO_4 instead of 0.1M for the same anodization conditions. After analysing the cross-section with the SEM, the alumina layer was found to not been stripped and with an abnormal sediment

formation near the surface (as seen in Figure 17). This issue persisted until the stripping solution was changed back to the original composition concentrations. This seemed to indicate that an excess of Na_2MoO_4 is detrimental to the stripping process and that the concentration limit that can be used is between 0.1M and 0.2M.

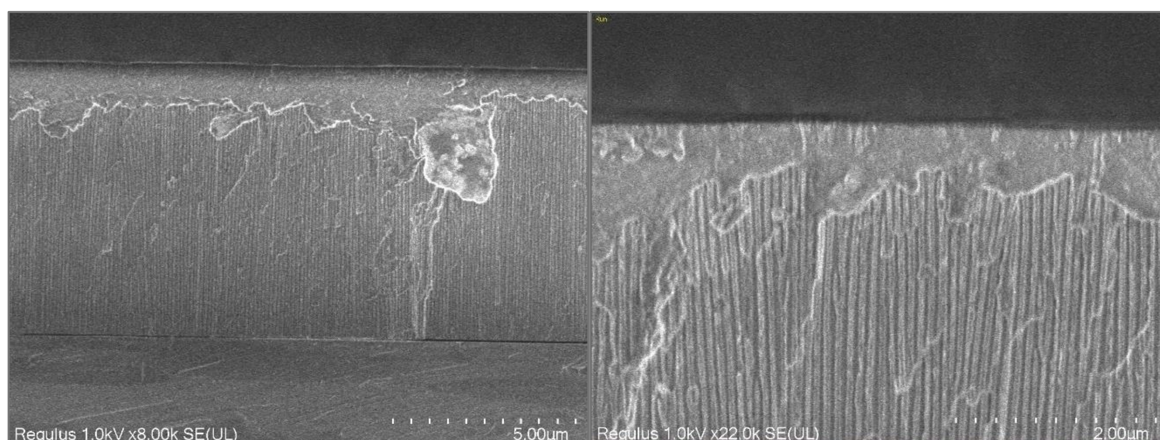

Figure 17: Cross-section SEM images of additional stripping test with 0.4M H3PO4 and 0.2M Na2MoO4.

3.3.6 Two-step anodization optimization

After individually testing each step, the full two-step anodization process is optimized. Test samples with aluminium (Al) deposited directly on top silicon (Si) are repeatedly anodized and examined to fine-tune the process as to obtain desirable results that can then be applied to the final samples with graphene. This optimization is performed on these preliminary samples because they are less costly and simpler to fabricate compared to the graphene containing samples.

Samples with 5 μm of Al on top of Si are chosen to begin with the optimization process. This aluminium thickness is selected as it offers a good starting point with which pore ordering conservation can be observed on the final mask without requiring very long first step anodization times.

1st two-step anodization

A first test is done with a 5 μm sample of an entire two step technique. Firstly, the process begins with one step of anodization done with 0.3M Oxalic acid at 40V and 15ºC during 70 min. This step anodizes approximately 4.2 μm of the layer of Al based on the speed calculated in the previous section. Then, the thick and disordered nanoporous alumina layer left by the first anodization is stripped away. The stripping is done by submerging the entire cell piece into a 0.4M H_3PO_4 and 0.1M of Na_2MoO_4 solution at 60ºC for 15 minutes while stirring moderately (300 rpm). Before and after the stripping step, the anode cell is rinsed with distilled water and dried with a nitrogen gun to minimize cross contamination between the acids.

After stripping, the sample is then anodized for a second time. This anodization is done under the same conditions as the first one as to obtain the same pore morphology and promote pore

ordering conservation (0.3M Oxalic acid at 40V and 15ºC). Despite the time needed to anodize the remaining 800 nm is around 14 minutes based on the previously calculated reaction speed, the second anodization step is done for 16.6 minutes. The extra time is given to guarantee all the aluminium is anodized so that the alumina layer sits directly on top of the Si layer.

The overview of the process is as follows:

· 1st anodization with 0.3M Oxalic acid at 40V and 15ºC during 70 min (650rpm)

· Stripping in 0.4M H_3PO_4 and 0.1M of Na_2MoO_4 solution at 60ºC during 15 min (300rpm)

· 2nd anodization with 0.3M Oxalic acid at 40V and 15ºC during 15 min (650rpm)

Figure 18.b) shows the SEM cross-section images of the sample near the top-side after the full two step. In the image, two distinct layers can be appreciated. One layer on top with vertical stripes that corresponds to the pores of the alumina layer, and another layer on the bottom that corresponds to the Si. The first thing to note is that no layer of aluminium can be observed between the two. This is a positive observation as any remaining aluminium would hinder in the step of plasma etching with a final graphene sample. Additionally, the thickness of the mask corresponds to the expected thickness based on the calculated speeds with less than a 20% error. The mask measures 1.08 µm on average and the expected thickness calculated at the beginning of the process with the anodization times was 1.28 µm.

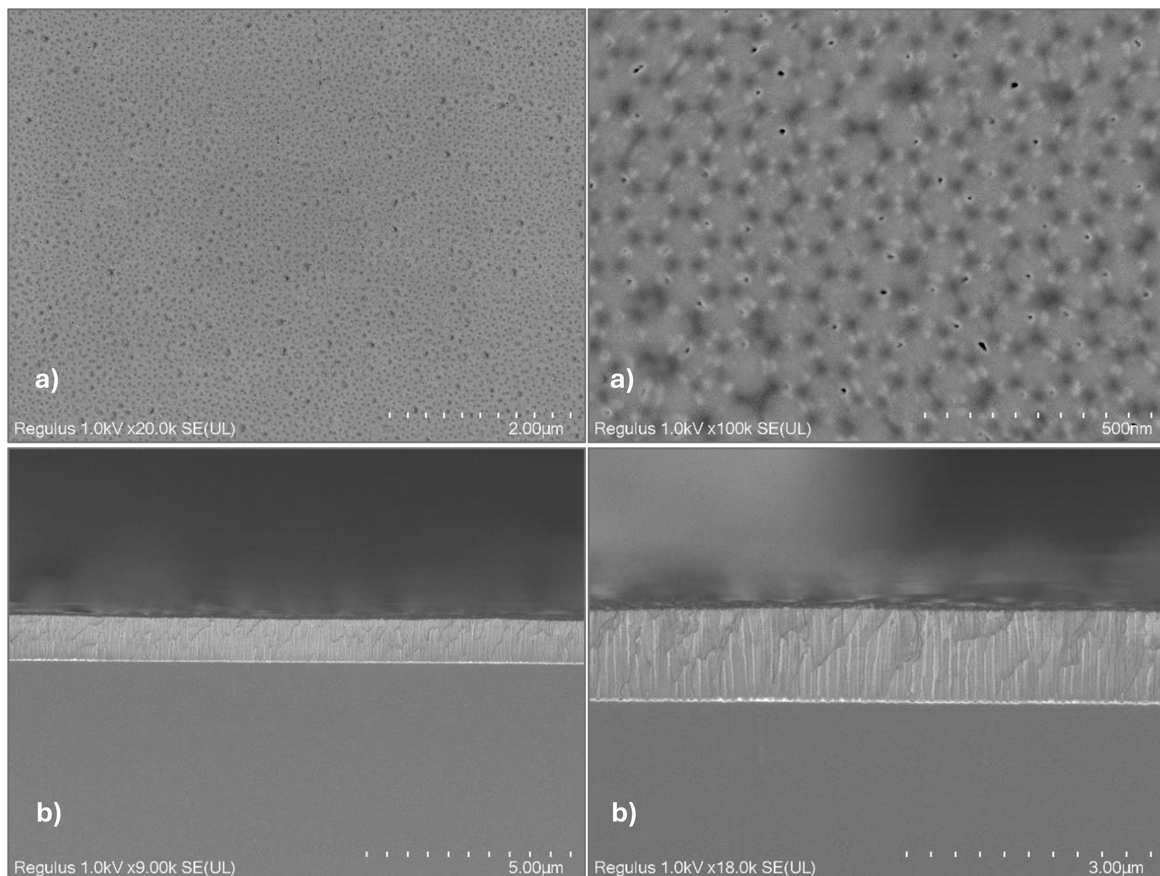

Figure 18: SEM images of Al-on-Si sample after 1st two-step optimization anodization. (a) SEM top-view images. (b) SEM cross-section images.

Figure 18.a) shows SEM top-view images. Faint hexagonal marks can be observed on the surface of the aluminium. These marks are traces of the texture left by the bottom of the pores of the first anodization. Despite these traces being present, it is clear that at least part of the texture is lost. The pores do not line up with the centre of the hexagonal markings, indicating that pore ordering was not conserved. Despite the positive results in regard to the thickness of the final alumina layer obtained, the pore ordering conservation requires improvement.

2nd two-step anodization - Pore widening test

Pore widening is a process that has been used in some anodization studies to adjust pore diameter [18], [46]. This is done by enlarging the pores after anodization with an etching treatment. Traditionally, the etching is performed with the same solution of the stripping process but at a lower temperature to allow for a higher degree of control.

Pore widening is a beneficial technique for the purposes of this work. Enlarging pores will reduce the pore aspect ratio of a given alumina layer and reduce the thickness of the oxide at their bottom. Both factors facilitate the use of the nanoporous alumina layer as a mask. After having tried a full two step process, a test of the pore widening test is done. A sample is prepared following the same process seen in the previous test. Subsequently, etching is done in a 0.4M H_3PO_4 and 0.1M of Na_2MoO_4 solution at 30ºC during 15 minutes while stirring. The full process overview is the following:

· 1st anodization with 0.3M Oxalic acid at 40V and 15ºC during 70 min (650rpm)

· Stripping in 0.4M H_3PO_4 and 0.1M of Na_2MoO_4 solution at 60ºC during 15 min (300rpm)

· 2nd anodization with 0.3M Oxalic acid at 40V and 15ºC during 15 min (650rpm)

· Pore widening in 0.4M H_3PO_4 and 0.1M of Na_2MoO_4 solution at 30ºC during 15 min (300rpm)

Figure 19.a) shows SEM top-view images of the sample before and after performing pore widening. It can be observed that the pores increase notably in diameter after pore widening. Pore diameter goes from around 30nm to 50nm approximately. These were the expected results, and they seem to indicate the technique works as intended.

When the cross-section in Figure 19.b) is observed, however, a problem can be spotted immediately. After performing pore widening, the pores seem to have lost their verticality. Stirring during this process is likely the cause for this. The strong turbulent flow of the etching solution causes the pores to etch in laterally and fuse with other pores creating branch-like patterns. It is clear after performing this test that stirring has a negative effect on pore widening.

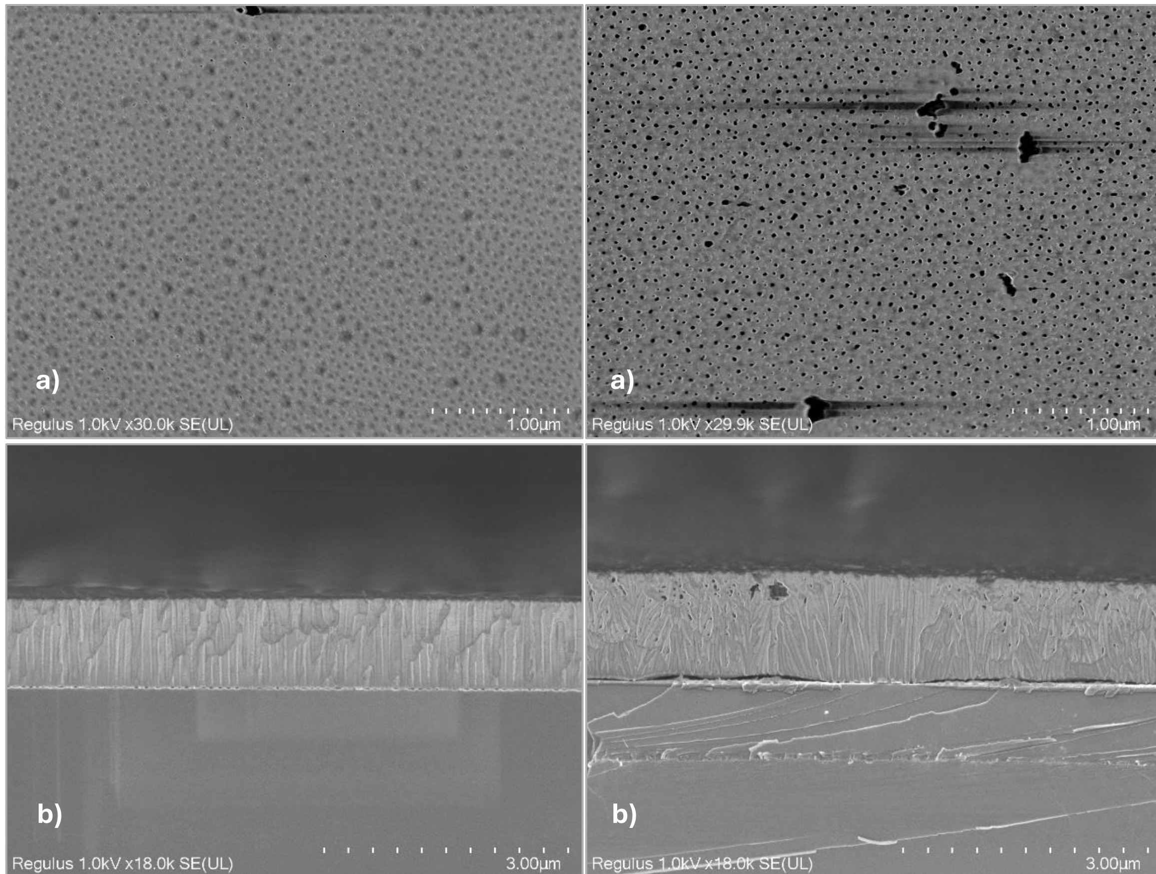

Figure 19: SEM images of Al-on-Si sample after 2nd two-step optimization anodization. (a) SEM top-view images. (b) SEM cross-section images.

3rd two-step anodization – Eliminating stirring from stripping step

Another full two step process test is done to attempt to solve the pore ordering issue observed on the first test. As stirring was found to be detrimental during pore widening, stirring during the stripping process could also be the cause of the loss of pore ordering. To test this hypothesis, the same process from the first test is performed again but without any stirring during the stripping test:

· 1st anodization with 0.3M Oxalic acid at 40V and 15ºC during 70 min (650rpm)

· Stripping in 0.4M H_3PO_4 and 0.1M of Na_2MoO_4 solution at 60ºC during 15 min (0rpm)

· 2nd anodization with 0.3M Oxalic acid at 40V and 15ºC during 15 min (650rpm)

The top-view images in Figure 20.a) show a disappointing result. Pore ordering is very poor despite the change in the stripping step. Additionally, the pores seem to have abnormally large pore diameters. This is unexpected because no pore widening steps were performed at the end of this process.

The cross-section images in Figure 20.b) reveal the cause for the unexpected results. By removing stirring from the stripping step, the stripping speed has slowed down, and 15 minutes are insufficient to completely remove the first anodization layer. As a result, the alumina layer

corresponding to the first anodization is still present. Looking at the picture, two different regions within the alumina layer can be observed. Each region corresponds to each of the two anodizations. In the x45k amplification, the transition between the wider pores of the first anodization to the thinner pores of the second one can be observed. The pores are thicker in the 1st anodization region because they were widened during the failed stripping process. An important detail to note, is that all pores from the second anodization begin at the bottom of the first anodization pores. That indicates pore ordering conservation was achieved under these conditions.

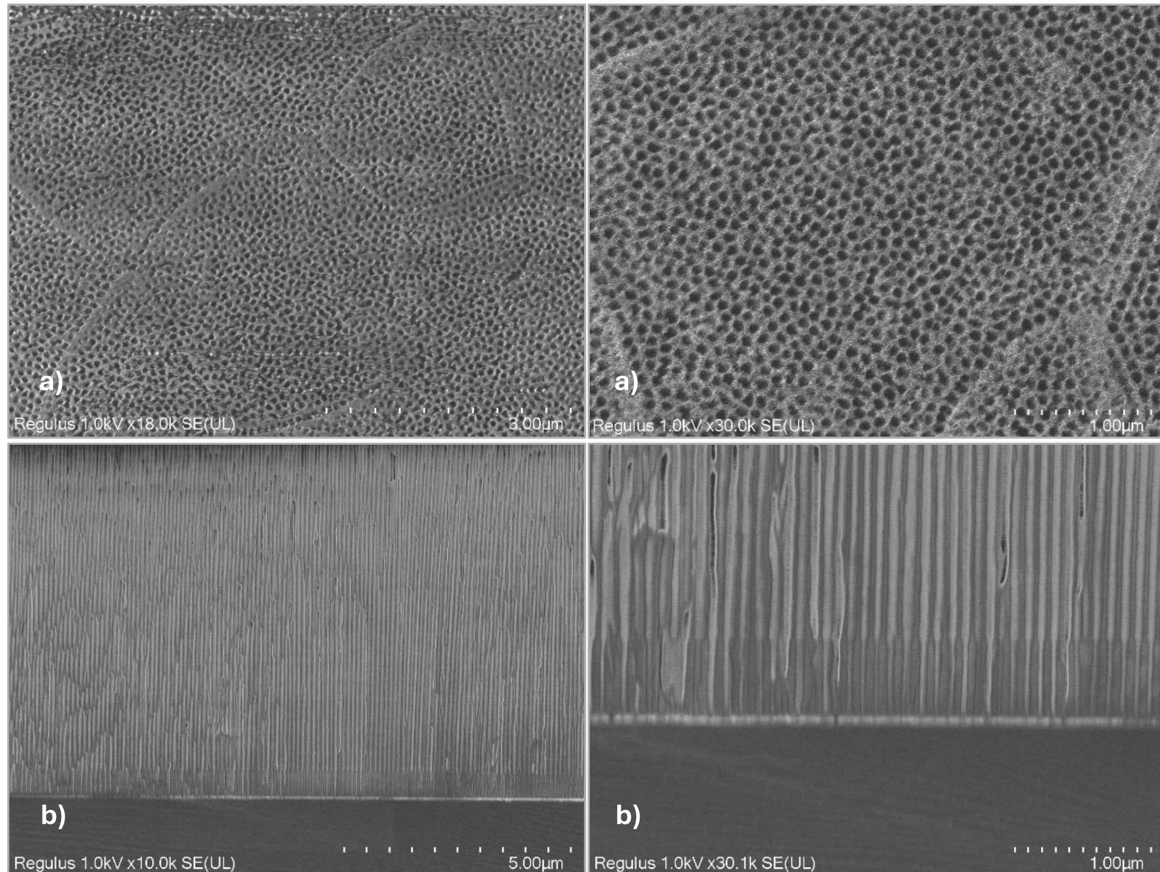

Figure 20: SEM images of Al-on-Si sample after 3rd two-step optimization anodization. (a) SEM top-view images. (b) SEM cross-section images.

4th two-step anodization – Increasing stripping time (15min to 30min)

A full two step process is repeated with no stirring during the stripping step. This time, however, the stripping time is increased from 15min to 30min. This is done to guarantee the first anodization alumina is fully removed before the second anodization commences. The overview of the full process is the following:

· 1st anodization with 0.3M Oxalic acid at 40V and 15ºC during 70 min (650rpm)

· Stripping in 0.4M H_3PO_4 and 0.1M of Na_2MoO_4 solution at 60ºC during 30 min (0rpm)

· 2nd anodization with 0.3M Oxalic acid at 40V and 15ºC during 15 min (650rpm)

The images of the cross-section in Figure 21.b) Show that the added time to the stripping step successfully solved the first anodization oxide prevailing issue. The thickness of the remaining alumina layer has the expected dimensions of ~1 µm.

Looking at the top view of the sample in Figure 21.a), nonetheless, shows that the pore ordering conservation issue is still present. Pores can be seen growing in a disordered manner, ignoring the hexagonal marks left by the preceding anodization. That indicates, unfortunately, that stirring was not the cause for the loss of ordering.

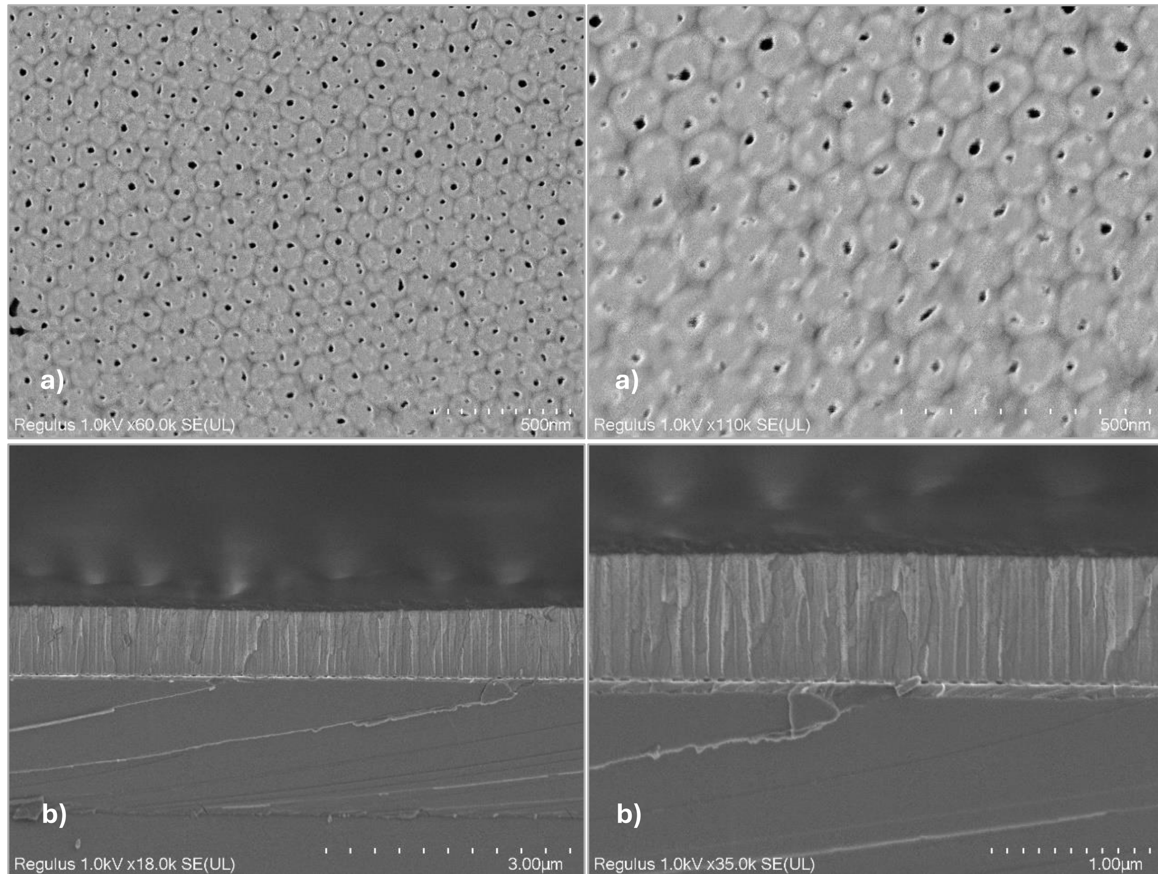

Figure 21: SEM images of Al-on-Si sample after 4th two-step optimization anodization. (a) SEM top-view images. (b) SEM cross-section images.

5th two-step anodization - Partial stripping technique

Pore ordering has not been successfully conserved in any of the two-step tests conducted up to this point, as the stripping solution damages the alumina surface upon contact. If the solution did not alter the surface texture, pore conservation could be achieved. This is supported by the results of the pore widening test, which indicate that the pores from the second anodization begin at the base of the partially dissolved pores from the first anodization.

Building on this observation, a new technique is proposed. Instead of completely removing the alumina formed during the first anodization, it will be only partially stripped as accidentally done in the 3rd two-step anodization. This approach ensures that the underlying aluminium remains intact, allowing for pore ordering to occur during the second anodization. To remove the

remaining alumina from the first anodization, another partial stripping step will simply be performed after the second anodization. This second partial stripping step, will not only remove the already half-etched first anodization alumina, but it will also widen the pores of the desired thin layer mask underneath. This is an added benefit as pore widening is desirable and would otherwise have had to be included as an extra step.

A two-step process implementing partial stripping is done first with a 5 μm Al sample:

· 1st anodization with 0.3M Oxalic acid at 40V and 15ºC during 70 min (650rpm)

· Stripping in 0.4M H_3PO_4 and 0.1M of Na_2MoO_4 solution at 60ºC during 17 min (0rpm)

· 2nd anodization with 0.3M Oxalic acid at 40V and 15ºC during 15 min (650rpm)

· Stripping in 0.4M H_3PO_4 and 0.1M of Na_2MoO_4 solution at 60ºC during 10 min (0rpm)

As shown in Figure 22.a), the technique has proven to be highly successful. The alumina layer remaining after the full process exhibits a distinct honeycomb pattern, with pores that are equidistant and arranged in a hexagonal configuration. Pore ordering was clearly well-preserved between the two anodizations. However, it is important to highlight the presence of broken areas scattered throughout the layer. Despite the high regularity of the nanoporous structure, these imperfections are present, and their potential causes will be addressed in the results of the upcoming optimization section.

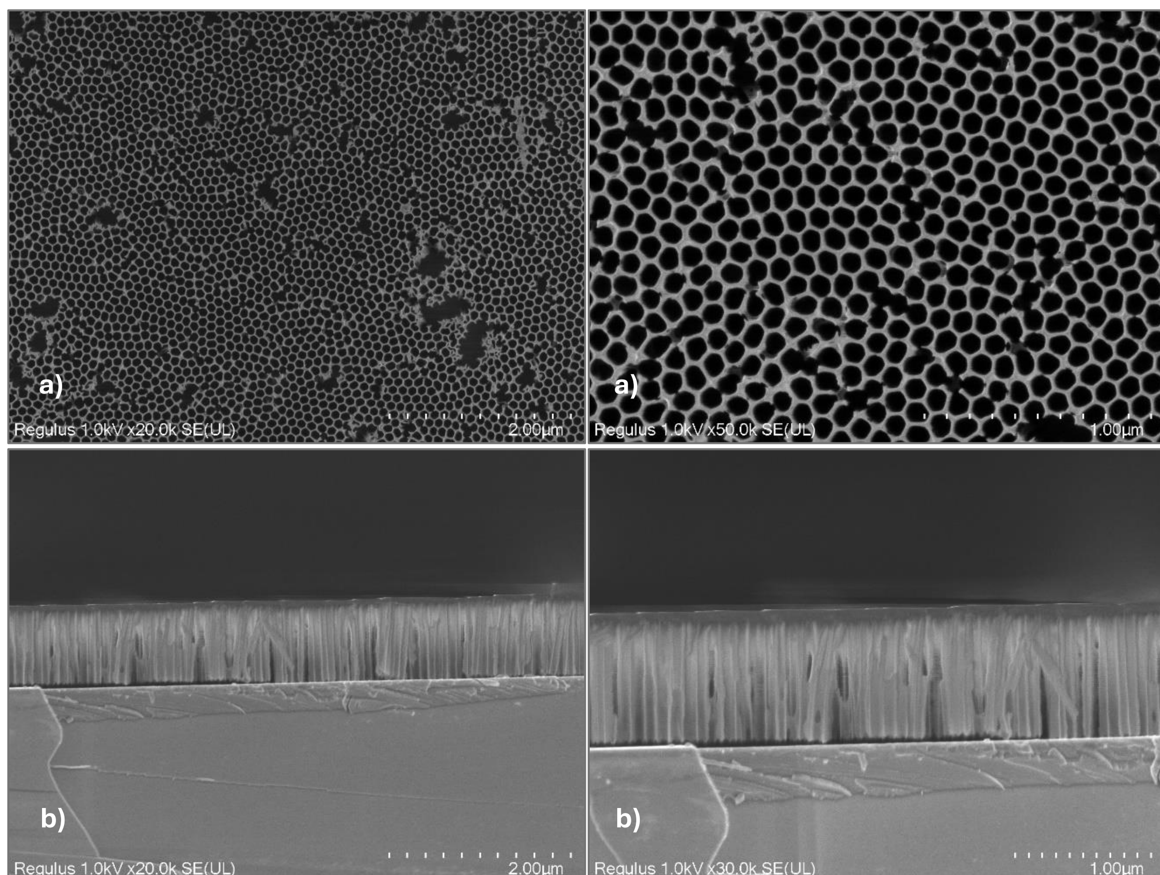

Figure 22: SEM images of Al-on-Si sample after 5th two-step optimization anodization. (a) SEM top-view images. (b) SEM cross-section images.

Examining the cross-section in Figure 22.b) reveals even more encouraging results. The layer has achieved the expected thickness corresponding to the second anodization time. Furthermore, the pores are fully open at the bottom, which is particularly advantageous. This openness simplifies the use of alumina as a mask, as it eliminates the need for an initial etching step to remove the remaining material.

6th two step anodization - Partial stripping with 10um

One parameter that has been shown to enhance pore ordering is the duration of anodization. The longer the first anodization process, the better the resulting alumina layer's pore ordering. With the development of the partial stripping technique, which successfully conserves pore ordering, it is now possible to evaluate pore ordering across different layer thicknesses. By using thicker initial aluminium layers, longer first anodization times can be achieved. To determine whether pore ordering can be significantly improved beyond the results obtained with the 5 μm aluminium sample, the partial stripping process is repeated now using a sample with 10 μm of aluminium deposited instead. Anodization times are modified accordingly to obtain a <1 μm thick final layer. Partial stripping times were also increased to account for the extra thickness produced by the first anodization. The overview of the process is as follows:

· 1st anodization with 0.3M Oxalic acid at 40V and 15ºC during 153 min (650rpm)

· Stripping in 0.4M H_3PO_4 and 0.1M of Na_2MoO_4 solution at 60ºC during 25 min (0rpm)

· 2nd anodization with 0.3M Oxalic acid at 40V and 15ºC during 15 min (650rpm)

· Stripping in 0.4M H_3PO_4 and 0.1M of Na_2MoO_4 solution at 60ºC during 10 min (0rpm)

The resulting alumina layer is highly compromised, with the porous structure severely damaged and deep cracks visible throughout, as it can be seen in Figure 23. These cracks appear to result from partially etched pores that have separated and collapsed. It seems that during anodization between the stripping steps, the pores formed in the first anodization—due to their high aspect ratios and weakened structural integrity after partial etching—have collapsed onto each other. This collapse has led to densely packed clusters of pore fragments, which obstruct the flow of the second partial stripping solution. As a result, most of the pores from the first anodization were not fully removed.

However, at the highest magnification, an interesting observation can be made. In the regions between the cracks, where no collapse occurred, the pores exhibit perfect ordering. In these areas, the etching solution flowed unobstructed, allowing the partial stripping to succeed. This suggests that partial stripping can be effective, but only up to a certain alumina layer thickness. If the first anodization produces an overly thick alumina mask, the pores are prone to collapsing after the initial etching, which disrupts the nanoporous structure. It is likely that the damage observed in previous tests was caused by uneven etching of the first anodization layer.

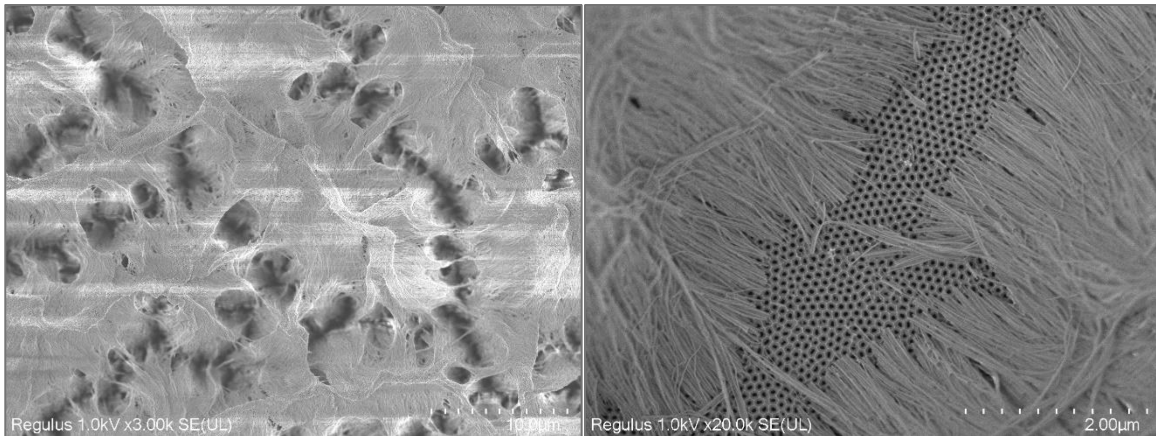

Figure 23: Top-view SEM images of Al-on-Si sample after 6th two-step optimization anodization.

7th two step anodization - Partial stripping with 875nm

To test this theory, partial stripping is tested with a much thinner sample. 875nm of Al are deposited on a Si wafer. Despite getting worse ordering with shorter first anodizations, if the process works well, there will be no broken areas, and there will be better ordering than in the first tests with thicker aluminium layers where pore ordering was not conserved. Additionally, doing a two step anodization on a thinner layer of aluminium also has the advantage of higher control of the final thickness of the mask. Final alumina layers of 200 or 300 nm can be easily achieved without the risk of consuming the entirety of the aluminium in the first anodization.

The overview of the process done is as follows:

· 1st anodization with 0.3M Oxalic acid at 40V and 15ºC during 9 min (650rpm)

· Stripping in 0.4M H_3PO_4 and 0.1M of Na_2MoO_4 solution at 60ºC during 12 min (0rpm)

· 2nd anodization with 0.3M Oxalic acid at 40V and 15ºC during 9 min (650rpm)

· Stripping in 0.4M H_3PO_4 and 0.1M of Na_2MoO_4 solution at 60ºC during 5 min (0rpm)

The results, shown in Figure 24, are highly promising. Although the degree of ordering is somewhat limited due to the brief first anodization period, pore alignment has been effectively preserved. The pores clearly originate from the cell texture formed during the first anodization step. This method seems to be the most effective approach for producing thin, ordered nanoporous alumina when access to chromic acid is not possible.

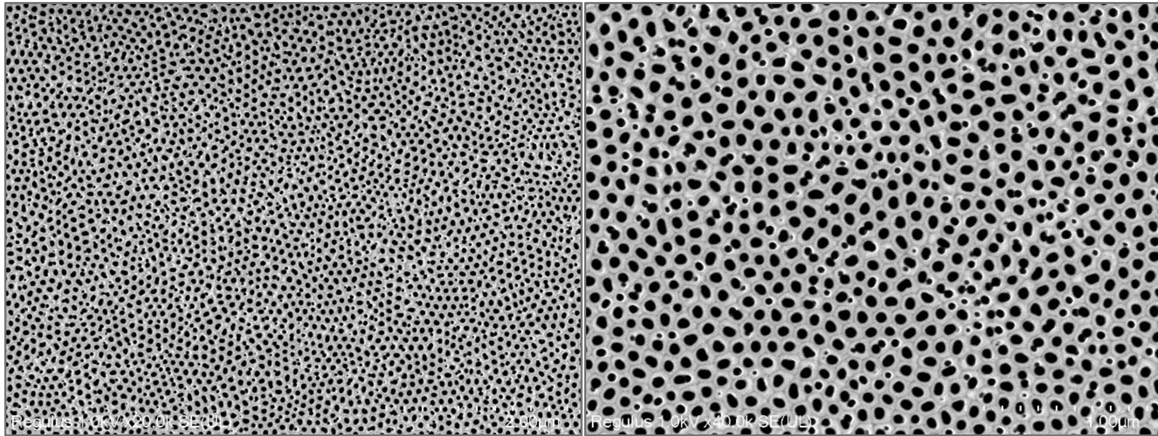

Figure 24: Top-view SEM images of Al-on-Si sample after 7th two-step optimization anodization. 20k augment: left image; 40K augment: right image.

Chapter summary

This subsection provides a concise summary of the work carried out to optimize the two-step anodization process. The primary goal of this optimization was to develop a method capable of producing an alumina mask with specific characteristics: a thin layer (~500 nm), some degree of pore ordering, and wide pores to facilitate plasma etching.

In the initial test, the target mask thickness was successfully achieved, but pore ordering was not observed. To address this, stirring was eliminated during the stripping step (third test), as it was hypothesized that turbulence might be disrupting the aluminium surface texture, as seen in the pore widening experiment. However, this adjustment did not resolve the issue.

Next, a partial stripping method was explored in the fifth test. In this approach, the alumina from the first anodization step is not completely removed, preventing the stripping solution from coming into contact with the aluminium surface. This technique was intended to preserve pore ordering, based on the promising results from the third test. The initial partial stripping experiment, conducted with a 5 μm aluminium sample, showed promising results with good pore ordering and the desired mask thickness. However, some areas of the alumina layer exhibited damage.

The areas with damage and defects increased when partial stripping was repeated with a 10um Al sample (6th test). This was attributed to the long pores of the first anodization alumina collapsing and forming clusters more easily the thicker the initial Al layer is.

Finally, partial stripping was tested on a thinner 875 nm aluminium sample, yielding extremely positive results that met all established criteria. Thus, partial stripping with a thinner initial aluminium layer was identified as the optimal anodization process for this work.

Table 1, found below, summarizes all the individual experiments done, with brief descriptions of the modifications done for each one, the purpose behind those modifications, and the main observed results.

ANODIZATION TEST ID	PURPOSE OF TEST	PROCESS MODIFICATION FROM PREVIOUS TEST	OBSERVED RESULTS
1st two-step anodization (TSA) 5um Al sample	Start two-step anodization optimization	-	· Final mask has adequate thickness · No Al remaining between layers · No pore ordering
2nd TSA – Pore widening (PW) test 5um Al sample	Testing pore widening step	·PW step introduced at the end of anodization process (30ºC; 15min; 300rpm)	· Pores widen from ~30 to 50nm · Pore verticality is compromised due to stirring while widening.
3rd TSA – Eliminating stirring from stripping step 5um Al sample	Attempting to fix loss of pore ordering	·Since stirring was detrimental in the PW test, stirring is also removed from stripping step ·PW is not done	· Final mask has unexpectedly high layer thickness due to lack of stirring while stripping for the same time (1st anodization alumina was not removed) ·Pore ordering is observed on the part of alumina corresponding to 2nd anodization
4th TSA – Increasing stripping time 5um Al sample	Removing alumina corresponding to 1st anodization step while retaining pore ordering	·Stripping time is increased from 15 to 30 min	·1st anodization alumina no longer prevails ·Pore ordering was not conserved
5th TSA – Partial stripping technique 5um Al sample	Attempting to fix loss of pore ordering	·First stripping step is done for an insufficient amount of time in purpose to prevent contact between stripping solution and aluminium ·PW step is added at the end to widen pores of final mask and remove alumina still remaining from 1st anodization	· Final mask has adequate thickness · Pore ordering is observed ·Alumina layer is slightly damaged
6th TSA – Partial stripping technique 10um Al sample	Testing effect of 1st step anodization duration on pore ordering of final mask	·Partial stripping is repeated only adjusting anodization times and stripping times to account for the extra Al thickness	· Exceptional pore ordering is observed on some areas · Some pores have formed clusters of debris due to high thickness of Al layer
7th TSA – Partial stripping technique 875nm Al sample	Fixing clusters issues by significantly reducing starting Al thickness	·Partial stripping is repeated only adjusting anodization times and stripping times to account for the extra Al thickness	·Satisfactory pore ordering is observed ·Alumina layer is free from defects or damage ·Final mask has desired thickness <500nm

Table 1: Summary of the anodization tests done to optimize two-step anodization. In the observed results column, black comments represent positive observations and red comments negative ones.

4 RESULTS AND DISCUSSION

4.1 CVD-grown graphene

After the graphene CVD growth process on Mo, Raman spectroscopy is performed using a Renishaw inVia Raman microscope with a 633 nm laser. This is done to verify the presence of graphene after the CVD process and to assess in a broad qualitative manner, the quality and characteristics of the grown graphene. The spectrum is measured for the frequency range of 1100 cm^{-1} to 3200 cm^{-1}. Multiple measurements are taken at different areas of the wafer to ensure the evenness of the grown graphene and representative results.

To determine the location, magnitude and width of the Raman bands, the spectra is fitted using the non-linear least squares curve fitting routines of Matlab [47]. Three Lorentzian curves are used for the fitting.

Figure 25 shows the Raman spectra obtained after CVD growth of graphene on the deposited Mo (shown in purple with the baseline removed), the fitted curves for the individual bands (green solid line), and the total fitting curve for the spectra (red line). As it can be seen, the three individual fitting curves found at 1338, 1585, and 2668 cm^{-1}, match the main characteristic bands expected when observing graphene, thus confirming its presence. The appearance of a D peak indicates that the graphene contains some defects. The I(G)/I(2D) ratio is approximately 0.6, and the 2D band has a full width at half maximum of 44 cm^{-1}. These characteristics suggest the presence of multilayered graphene of ~10 layers. Overall, the spectra confirm that defected multilayered graphene was synthesized on the Mo after the CVD growth process.

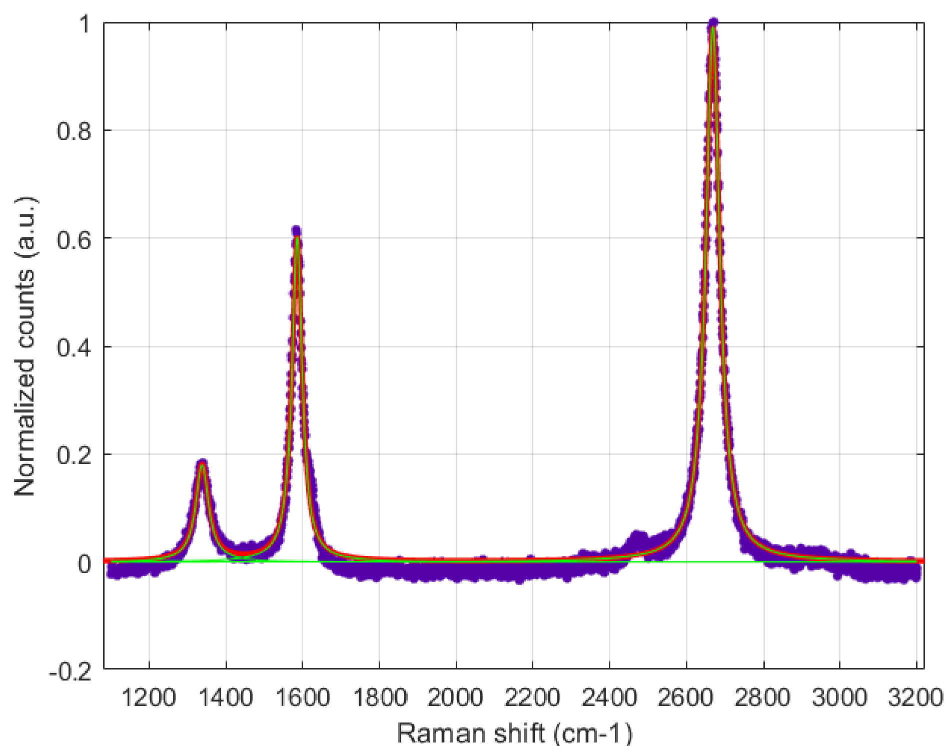

Figure 25: Fitted Raman spectra of graphene after Mo CVD growth measured with a 633nm laser. Original spectrum: purple dots; Fitted curves for individual bands: green solid line; Total fitting curve: red solid line.

4.2 Anodization on graphene

After having assembled the set-up and optimized the anodization process to produce the best results possible, anodization is finally performed on samples with graphene on them. Two graphene samples are anodized. Firstly, anodization is done on a sample with a thick 10um layer of Al. This sample is prepared by sputtering Mo on a wafer with a protective layer of SiO_2, then synthesising graphene on top of it by CVD, and finally, by sputtering the Al on top of the graphene. Anodization is done following a two-step process like the one done at the start of the optimization process (4th optimization test), but with appropriate times for the initial thickness difference. The purpose of this sample is to serve as a control with which to compare the results. The complete overview of the anodization process performed is the following:

· 1st anodization with 0.3M Oxalic acid at 40V and 15ºC during 153 min (650rpm)

· Stripping in 0.4M H_3PO_4 and 0.1M of Na_2MoO_4 solution at 60ºC during 30 min (0rpm)

· 2nd anodization with 0.3M Oxalic acid at 40V and 15ºC during 15 min (650rpm)

Secondly, a sample with 1000nm of Al thickness is anodized. The sample is prepared by sputtering Mo on a wafer with a protective layer of SiO_2, patterning that Mo, then synthesising graphene by CVD only on the centre area of the die where the Mo is, and finally sputtering the Al on top of the graphene. Mo patterning is done to this sample to improve adhesion as explained in the flowchart section. Anodization is performed following the most optimized partial stripping two-step anodization variation. This process should form a layer of alumina with large and ordered pores that behaves the best as a hard mask in a plasma etching process. The overview of the anodization process performed is the following:

· 1st anodization with 0.3M Oxalic acid at 40V and 15ºC during 11 min (650rpm)

· Stripping in 0.4M H_3PO_4 and 0.1M of Na_2MoO_4 solution at 60ºC during 12 min (0rpm)

· 2nd anodization with 0.3M Oxalic acid at 40V and 15ºC during 11 min (650rpm)

· Stripping in 0.4M H_3PO_4 and 0.1M of Na_2MoO_4 solution at 60ºC during 5 min (0rpm)

Regular Two-step anodization - 10 µm

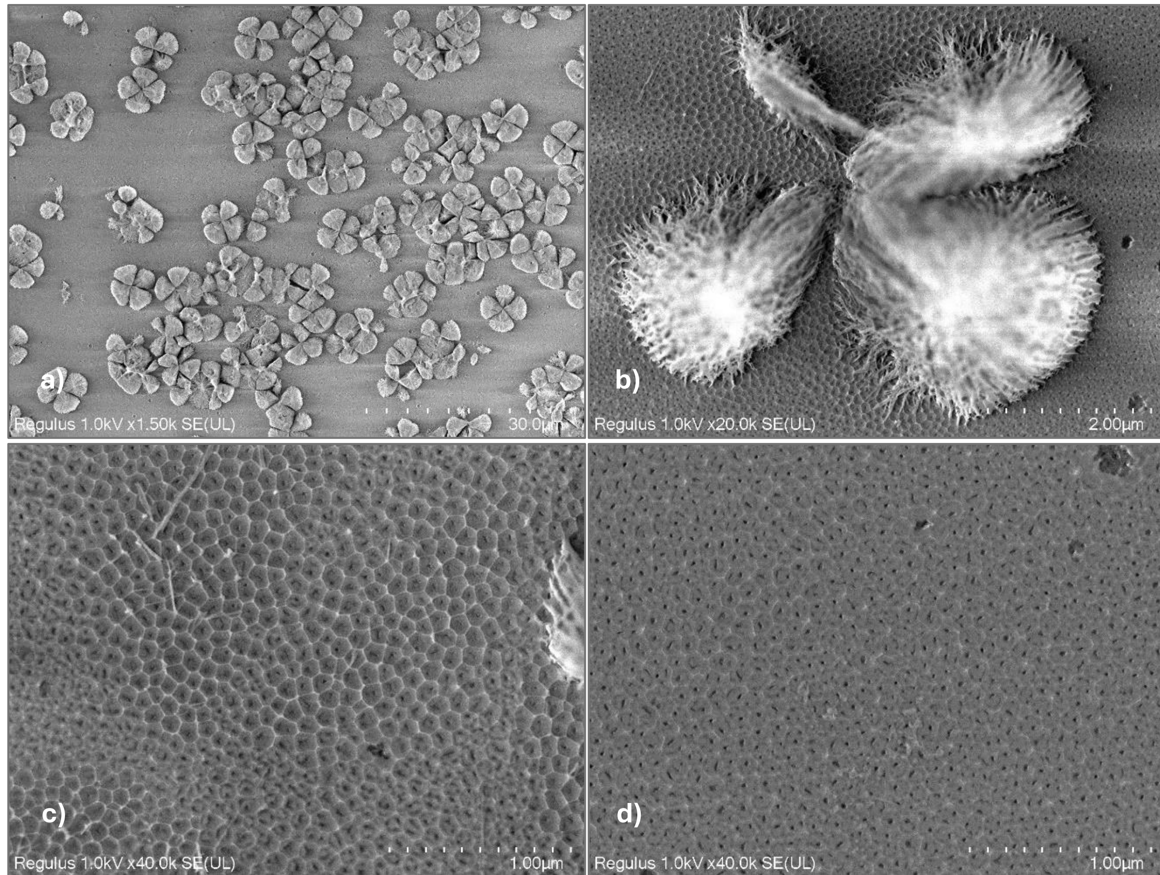

Figure 26: Top-view SEM images of first graphene containing sample after regular two-step anodization. (a) Low magnification overview of the sample's surface. (b) Close up image of clover-shaped structure. (c) Close up image of area with unordered pores. (d) Close up image of area with ordered pores.

In Figure 26, four top-view SEM images of the first graphene sample at different magnifications after anodization can be observed. As it can be seen in Figure 26.a), after anodization, abnormal clover-shaped structures can be seen scattered throughout the surface. Taking a closer look at them, in Figure 26.b), these structures seem to be clusters of partially etched pores that have bundled together. This is most likely due to the effect described in the second partial stripping experiment of the anodization optimization section. As the long pores of very thick alumina layers etch away in the first stripping step, they become structurally weak, and collapse. Once they collapse, it is harder for the stripping solution to etch those pore clusters, and the surrounding areas are etched first.

Traditionally, stripping is done for more time than needed to make sure all alumina is gone. This prevents the pore cluster problem altogether. However, when the stripping solution is made without chromic acid, such as in the case of this thesis, stripping the pores for too long causes the aluminium surface to lose its texture, losing pore ordering conservation in the process, and making the two-step anodization process a pointless endeavour. This already was the case for the pores in some areas of this sample as it can be seen in Figure 26.d). Most of the surface of the sample has lost the honeycomb texture and pores form in a very disordered manner. Interestingly, the areas close in proximity to the clusters have retained their texture, as evidenced by Figure 26.c). This is coherent with the hypothesized mechanism that is believed to

form the clusters. The areas next to them have been exposed less time to the stripping solution and, therefore, the texture has been preserved better.

Overall, it is clear that thick Al layers as a starting point to create transfer-free alumina masks are not a viable option with the etchant limitations had during the realization of this work. The results of this experiment show that aluminium texture is lost before all the first anodization step alumina debris can be removed. Therefore, with thick starting Al layers, after performing two-step anodization, either clusters would be present, texture on the aluminium would be lost, or both.

It is important to note that during anodization, intense bubbling between the layer of Al and graphene occurred. This caused severe delamination for most of the surface of the sample, creating wrinkles and disrupting the anodization process

Partial stripping - 875 nm

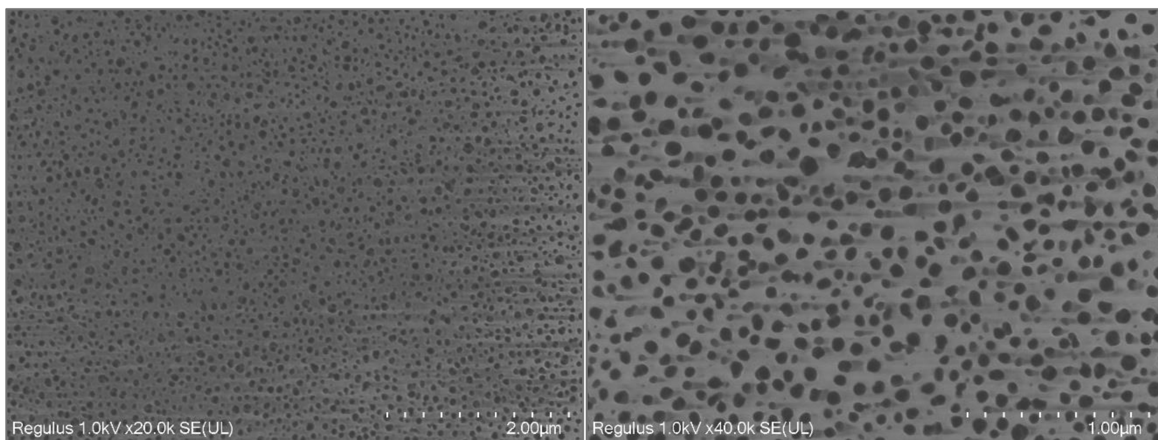

Figure 27: Top-view SEM images of second graphene containing sample after partial stripping two-step anodization.

In Figure 27, two top-view SEM images of the second graphene sample after anodization can be observed for different magnifications. The pores in this sample can be easily spotted as their diameter size is considerably bigger due to the second stripping step of the partial stripping process performed. Unfortunately, it can be observed that ordering was not conserved. The primary reason as to why this happen is believed to be bubbling. Just like for the previous sample, during anodization, the Al layer formed bubbles with anodization and stripping solution that entered between the Al and the graphene layer. This seems to have interfered with the anodization process.

Overall, while there is no pore ordering conserved, this sample presents an improvement compared to the previous one. No clover-shaped alumina structures are present, and, thanks to the patterning step during sample preparation, the bubbling of the Al was not as severe. For these reasons, even though the mask quality after following this process is less than ideal, the partial stripping sample is deemed as the better of the two, and the one chosen to test plasma etching with.

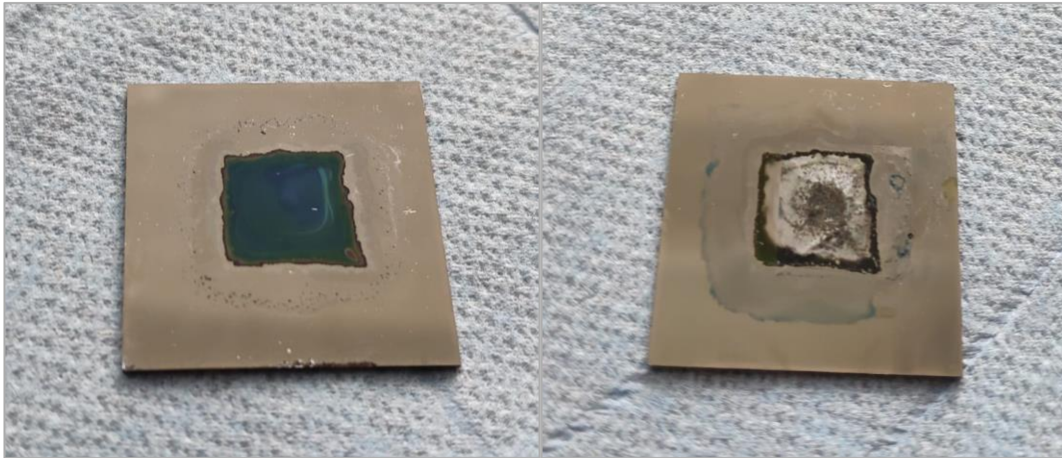

Figure 28: Image of Al-on-Si sample(left) and graphene containing sample (right) after performing anodization. Severe bubbling and wrinkling can be observed on the alumina of the graphene containing sample.

4.3 Plasma etching

Plasma etching is a pivotal technology in the field of microfabrication, crucial for producing intricate and precise patterns on semiconductor wafers and other substrates. This technique utilizes plasma—a highly ionized gas composed of ions, electrons, and neutral species—to selectively remove material. The plasma is typically generated by applying an electric field to a low-pressure gas, such as fluorine-bearing gases (e.g., CF_4 or SF_6), chlorine, or oxygen, which ionizes the gas and creates a reactive environment.

In plasma etching, the reactive species in the plasma interact with the substrate to break molecular bonds and form volatile byproducts that are easily evacuated. This process allows for both chemical and physical etching, enabling the creation of fine, detailed features with high precision. By adjusting parameters like gas composition, pressure, and power, plasma etching can be tailored to achieve specific etching profiles, whether for rapid material removal, high selectivity between different materials, or the formation of vertical features with sharp sidewalls.

In this thesis, plasma etching is used to pattern graphene with a transfer free alumina mask. Plasma etching is also done on the Al-on-Si test samples to test the transfer free alumina mask method when there is good layer adhesion. The best anodization method found during the process optimization phase did not produce the same results for the graphene samples due to adhesion issues. For that reason, it is important to see how well transfer free alumina can work as a mask when the mask conditions are ideal. All samples are etched using reactive ion etching with the commercially available Adixen AMS110 inductively coupled plasma (ICP) chamber.

For the patterning of Si, a premade recipe tailored for PDMS ething is used. This recipe pulses 200 sccm SF_6, 50 sccm O_2, and 150 sccm Ar at 2000W source power and 80W chuck power. Temperature at the chuck is kept at -10ºC and pressure throughout the process is 18.75 mTorr. This recipe is chosen because of its ability to etch alumina oxide as well as Si. In this work, the thickness of alumina at the bottom of the pores of the mask after anodization varies depending on the process followed. For those masks which have closed pores at the bottom, it is

important the plasma etching process can etch through them. The gas mixture of SF_6 and Ar at similar flow rates has been found to be one of the most effective compositions for reactive ion etching of alumina oxide [48]. Etch rate of alumina increases with the chuck power used. Moreover, the higher the chuck bias, the more ion-assisted etching increases, and the more anisotropic the etching is [49]. 80W of chuck power is chosen as that is the highest chuck power allowed by the tool owner at the cleanroom due to concerns of Al being sputtered from the edges of the die and depositing on the chamber.

Two tests are done for samples with Al on Si. First, a 10µm Al sample that has undergone the regular two step anodization alumina mask is tested. The alumina layer on the sample is less than 500nm thick and has the original pore diameter size grown with the used anodization conditions (0.3M Oxalic acid at 40V and 15ºC). Pore ordering in the sample is poor due to the problems described in the anodization process optimization section. This sample is etched using the recipe described above for 10 min.

Secondly, two 875nm Al samples are tested. Both of these samples are prepared using the partial stripping technique described in the last experiment of the anodization optimization process. The alumina layer on the samples is also less than 500nm thick and the pores are slightly enlarged due to the second stripping step of the partial stripping process. Plasma etching with the same PDMS recipe is performed on the samples for two different durations. One sample is etched during 2.5min while the other is etched during 15s. The objective of these test is to assess how well transfer-free alumina can work as a mask in Si, as well as comparing the difference in results between alumina that has undergone pore widening after anodization and alumina that has not. All samples are cut in half with a diamond pen and observed with SEM.

For the patterning of graphene, 200 sccm of O_2 flow is used, at 1500W of source power and 20W of Chuck power. O_2 plasma can etch the graphene while leaving the Mo underneath intact. It is important that the Mo is not removed in order to prevent the layer of graphene and alumina from detaching from the sample.

Etching is done on a sample prepared following the partial stripping method described in the anodization section. This sample also possesses a less than 500nm thick mask, with pores that are enlarged. 1 minute of O_2 plasma etching is performed. Results are observed with SEM.

4.3.1 Aluminium on silicon samples

Regular two step anodization – 10min etching

Figure 29 shows the cross-section of the 10µm sample after 10min of plasma etching. As it can be seen, wells have formed in the Si layer, right underneath the alumina mask. These wells are varying in size and are spread very unevenly throughout the surface of the sample. Some pores have not opened after the 10 min of plasma etching, while others have early in the process, leading to the unevenness. While not ideal, these results show promise and prove that transfer-free alumina can be used as a mask.

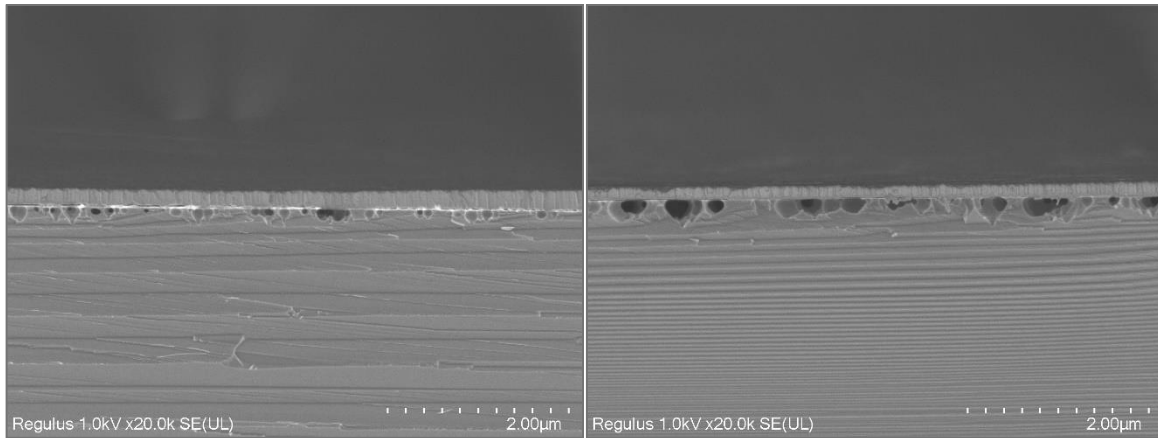

Figure 29: Cross-section SEM images of Al-on-Si sample with regular two-step anodization alumina mask after 10min of plasma etching with SF6 containing recipe.

Partial stripping - 2.5min etching

Figure 30 shows the cross-section of the 875nm sample after 2.5min of plasma etching. The etching process is the same as the one performed on the regular two-step anodization sample but 4 times shorter in duration. This was chosen as the pores of the partial stripping samples have been enlarged by the second etching step of the partial stripping process and the bottom of the pores is expected to offer much less resistance to the plasma if any at all. As it can be seen in the images, a large gap of ~2μm separates the alumina layer and the Si layer. The plasma has consumed all of the Si directly underneath the mask, causing the alumina layer to completely detach and forming a floating membrane. This makes evident that the alumina mask did in fact offer less resistance to the plasma compared to previous test.

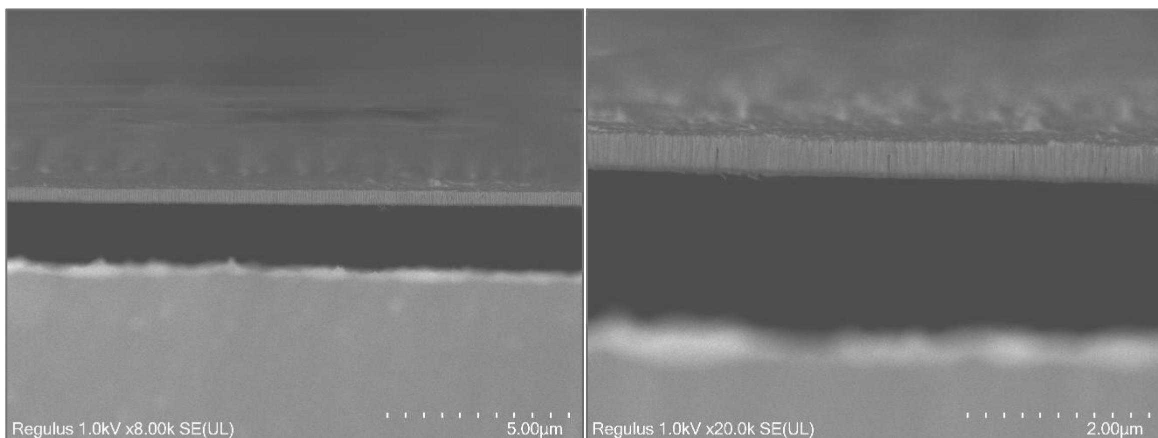

Figure 30: Cross-section SEM images of Al-on-Si sample with partial stripping two-step anodization alumina mask after 2.5min of plasma etching with SF6 containing recipe.

Partial stripping – 15s etching

Figure 31 shows the cross-section of the 875nm sample after just 15s of plasma etching. Multiple wells in the Si can be observed underneath the alumina layer. Unlike the ones observed

in the 10min etching sample with a regular two-step anodization fabricated mask, the ones found in this sample are very homogenous and equal in size. Moreover, they are present under almost all of the observed individual pores. This suggests the bottom of the pores is left completely open when following the partial stripping method.

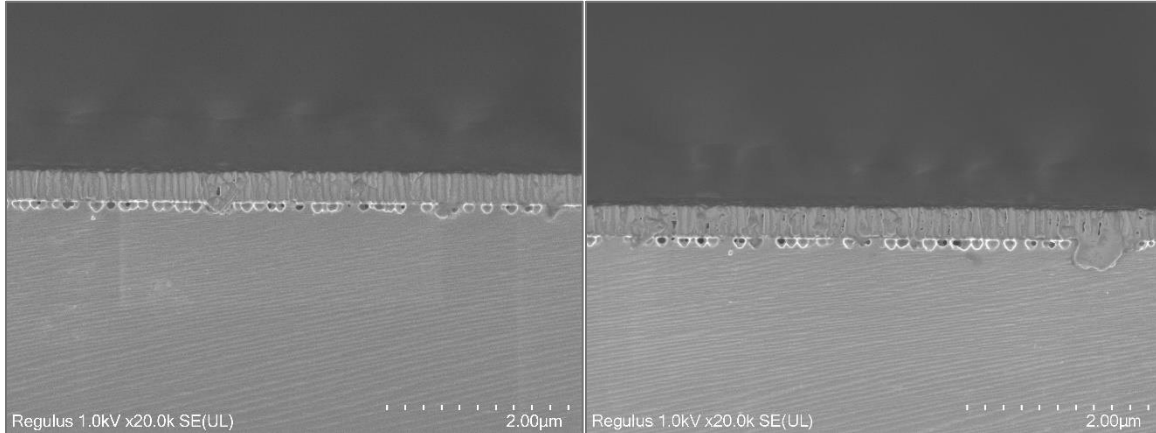

Figure 31: Cross-section SEM images of Al-on-Si sample with partial stripping two-step anodization alumina mask after 15s of plasma etching with SF6 containing recipe.

It is clear that with the stripping conditions used in the partial stripping process, the bottom of the pores of the mask is open at the end of anodization. This is beneficial because it greatly improves the evenness of the patterning. Even if the plasma recipe used can etch through alumina, such as the recipe used in this work, due to the variability of the bottom thickness of the pores and the slower etching rates of alumina compared to Si, the resulting patterning using an alumina mask with the pore bottoms intact is very irregular with a lot of depth variation, as shown in the 10min of etching test. This is specially a problem if the dry etching technique used is isotropic. The wells formed under the pores will quickly fuse into each other and grow very large in some areas, while on others there will be no wells formed, resulting in a pattern that does not resemble the morphology of the mask.

In summary, the results observed in the Al-on-Si plasma tests show that transfer-free alumina can be used effectively as a mask when adhesion between layers is good and a pore widening step is done during anodization.

4.3.2 Graphene sample

In this section, the results of the plasma etching process done on the graphene sample are presented. It is important to highlight that neither one of the graphene samples anodized behaved as expected based on the optimization tests done with Si. Both samples experienced severe delamination of the aluminium layer when anodizing, which compromised the pore formation process and the underlaying graphene sheet. Several attempts to get better results were made for both samples but the same severe delaminating behaviour was observed. This makes evident that the followed method in this thesis in its current form is not a viable process to generate low defect large area GNM. However, to assess the degree of success of this

process, and also to determine the best plan of action for future works, plasma etching is done on the graphene samples despite the suboptimal anodization results.

Since anodization electrolyte and stripping solution penetrated the alumina layer and made contact with the graphene sheet during anodization, two tests are done before plasma etching to verify there is graphene left on the sample. Firstly, Raman spectroscopy is performed on the sample to look for traces of graphene. Just like when verifying presence of graphene after CVD growth, a 633nm laser was used as a source, and the spectrum was measured for the frequency range of 1100 cm^{-1} to 3200 cm^{-1}. The spectra is once again fitted with three Lorentzian curves using Matlab's non-linear least squares curve fitting routines.

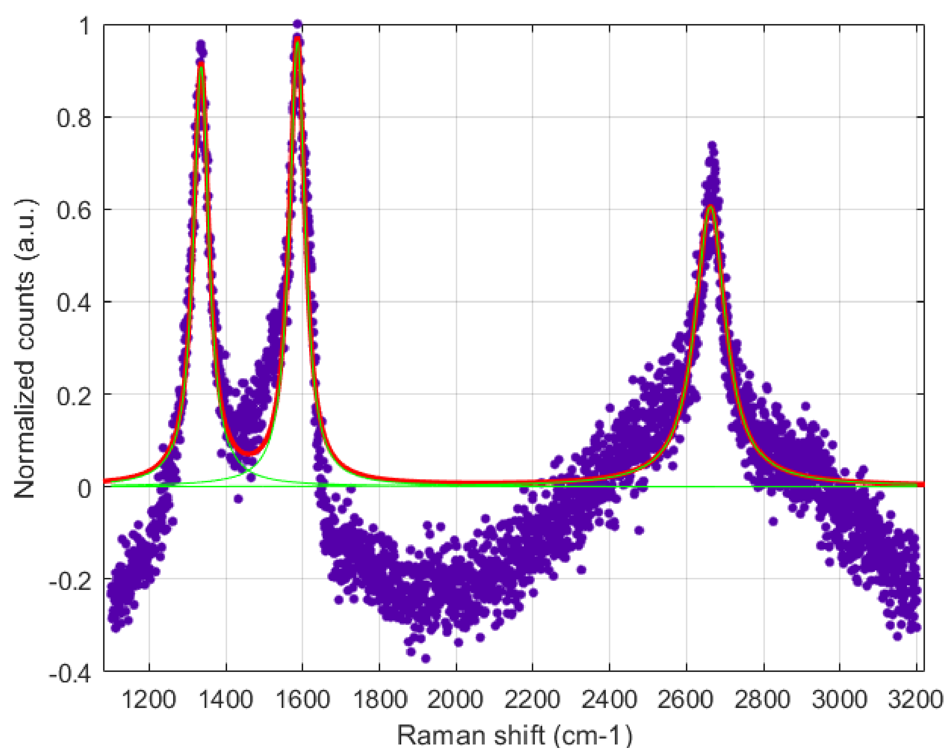

Figure 32: Fitted Raman spectra of graphene after Mo CVD growth measured with a 633nm laser. Original spectrum: purple dots; Fitted curves for individual bands: green solid line; Total fitting curve: red solid line.

Figure 32 shows the fitted Raman spectra obtained after preforming the measurement through gaps on the alumina layer of the sample. Despite the intense background signal, three curves are fitted at 1335, 1586, and 2662 cm^{-1}. These frequencies once again match the main band locations expected when observing graphene. This confirms that graphene survives the anodization process despite the aluminium layer partial delamination.

To better assess the quality of the graphene and Mo layers, an inspection is then done with the SEM. With the help of some metallic tweezers, part of the alumina layer is peeled off the centre part of the sample. The exposed part is then examined with the microscope.

Figure 33 shows the SEM topview images of the sample at two magnifications. In the images, a texture pattern can be observed throughout most of the surface. This texture is the typical

pattern expected for when observing a layer Mo covered with graphene. This seems to indicate that both layers have endured anodization well and are mostly intact despite the bubbling.

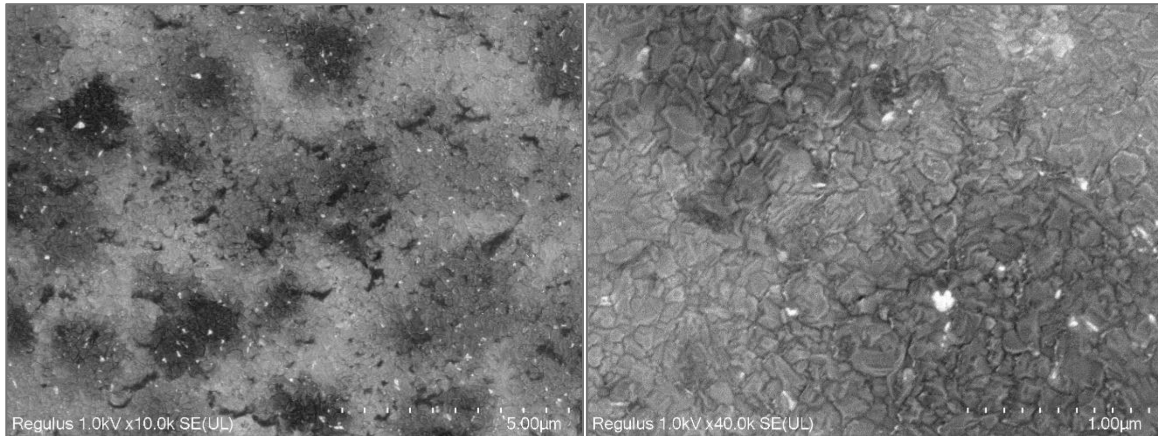

Figure 33: SEM top-view images of the second graphene containing sample after anodization and mechanically removing the alumina layer.

Having verified the presence and quality of the layers of Mo and graphene, 1 minute of oxygen plasma is performed as described in the experimental methodology section.

Plasma etching is done to the sample with part of the alumina mask still on. After the etching process, the entire alumina layer is removed, and then the sample is inspected on the area covered by alumina during the etching. Figure 34 and Figure 35 show two top-view SEM images taken of the sample on that area. Each figure represents one of two types of regions observed inside the area of interest.

Figure 34 shows the first type of region observed. In this region, the distinct texture of Mo covered by graphene can be seen. A pattern of irregular bright shapes is scattered through out the surface of the texture. It is believed these shapes correspond to defects on the multilayer graphene sheet, which let the bright shade of the Mo underneath shine through. Unfortunately, these shapes are too irregularly shaped and sized to be associated to holes or defects made by the oxygen etching through the pores of the alumina mask. It is possible they were made by big defects on the mask that caused uneven etching, or they could belong to defects in graphene that were present already before etching. In any case, it is clear that there are some regions on the area of interest of the sample, where the graphene sheet was not etched following the pattern of individual pores of the alumina mask.

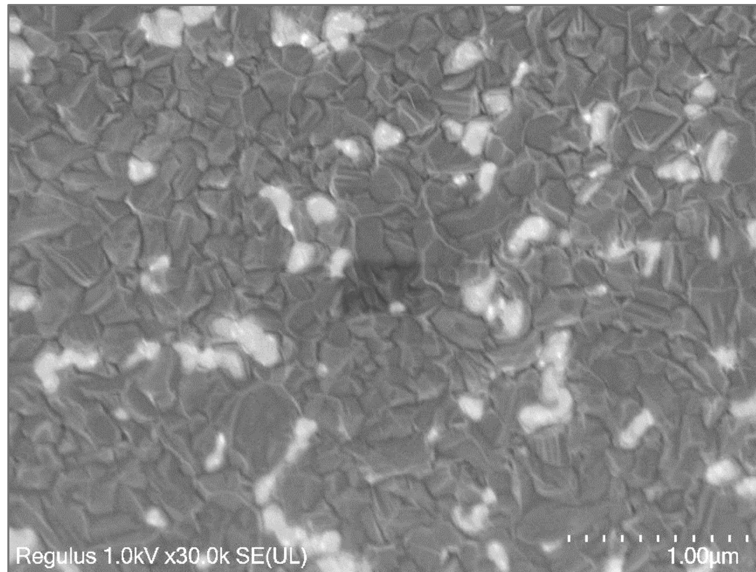

Figure 34: SEM top-view image of the second graphene containing sample after plasma etching and mechanically removing the alumina layer. Region with no spotted marks.

Figure 35 shows the second type of region observed. In some parts of the area of interest of the sample, as well as the big bright shapes discussed in the previous figure, smaller spots can be seen. These spots are rounder than the other shapes and are scattered closer together. Looking at the image, it seems possible that plasma etching with the alumina mask was successful on some areas and that these spots are the result of etching done through the pore pattern of the mask.

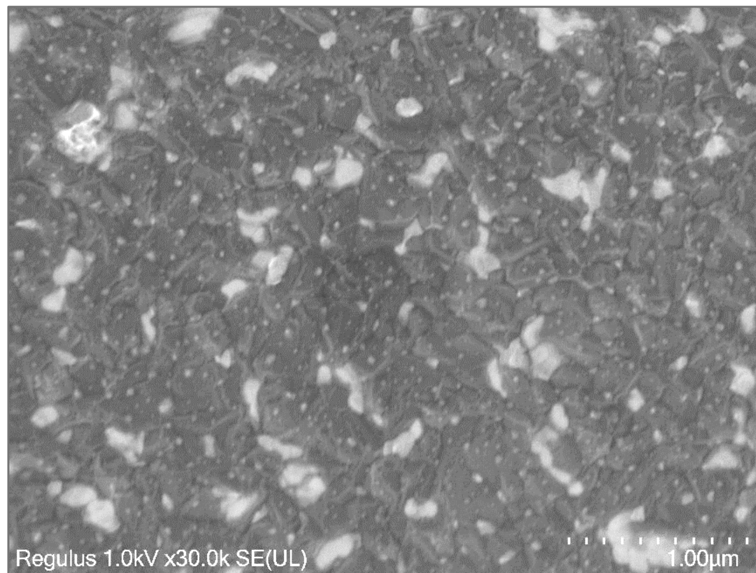

Figure 35: SEM top-view image of the second graphene containing sample after plasma etching and mechanically removing the alumina layer. Region with spotted marks.

To make a better assessment of this hypothesis, A Welch's t-test (α=0.05) is performed to determine if there is a statistically significant difference between the mean interpore distance of the alumina mask, and the mean distance between the spots observed in Figure 35. A sample of 50 measurements is taken from both the image of Figure 35, and the image of partial stripping alumina of Figure 24. The images and the measurements taken can be seen in more detail in the second section of the appendix.

The obtained means for the alumina interpore distance and spot distance are 82.6 nm and 79.9 nm respectively. The Welch's t-test reveals that there is no significant evidence of a difference in mean interpore distance ($t = 0.77$, $p = 0.44$) between the sample groups. While this result does not confirm the means are significantly equal, based on the results it seems likely the spots observed on those regions belong indeed to etch patterns created by the pores of the mask.

All in all, it is clear the process followed in this work is not adequate to produce good quality GNM sheets in a reliable manner. It is possible to achieve patterning with an alumina transfer-free mask in some areas of the graphene, but delamination issues make the patterning very unreliable and uneven. Future work should focus on fixing these delamination issues. As shown in the previous section, the process proposed in this thesis can work effectively when the aluminium layer has good adhesion with the layer underneath.

5 CONCLUSIONS AND RECOMMENDATIONS

Despite its remarkable electrical properties, graphene has not been used as a channel material in field-effect-transistors due to its 0eV band gap. Engineered graphene solutions such as graphene nanoribbons have been proposed. However, despite their opened band gap and great current on/off ratios, nanoribbons have very low individual driving currents.

Graphene nanomesh offers a solution to this problem. This alternative form of engineered graphene has the same advantages that nanoribbons present, but with higher driving current due to its two-dimensional nature. Unfortunately, the main methods used for its fabrication are challenging.

In this work, fabrication of graphene nanomesh was explored using alumina as a hard mask in a plasma etching process. Fabricating the alumina and then transferring on top of the graphene has been attempted before. However, cracking of the alumina was observed during transfer due to its brittle nature. In this thesis, a transfer-free approach is tested instead by depositing aluminium on top of graphene and performing anodization directly on the die.

For the anodization part of the process, a custom setup was developed with multi-jet-fusion (MJF) polypropylene 3D printed pieces as holders for the electrodes of the electrolytic cell. The holder for the anode worked adequately, but the holder for the cathode had issues initially. In the cathode, the die had to be housed in a water-tight seal that would allow only the surface of the aluminium to contact the electrolyte. A two-o-ring mechanism was used in the first design of the piece to achieve this seal. However, the rough surface finish of MJF was found to cause irreparable leaking issues. In the end, a successful seal was achieved on the third redesign by using EPDM foam instead of o-rings.

To fabricate the transfer-free mask, a two-step anodization process was followed. A series of tests of this process were performed on dies with only aluminium on silicon (Al-on-Si) to optimize it. The stripping step of the process was done with 0.4M H_3PO_4 and 0.1M Na_2MoO_4 instead of the traditionally used 0.4M H_3PO_4 and 0.2M H_2CrO_4 due to the unavailability of chromic acid. Unfortunately, this modification to the stripping solution caused the alumina to lose its texture given by the first anodization after the stripping step. To preserve the texture and achieve ordering conservation despite this issue, a partial stripping variation of the two-step anodization was developed. With partial stripping, the stripping solution does not contact aluminium at any point, and as such, pore ordering conservation was observed. However, it was found that this process variation has an initial aluminium thickness limit. Thicker than ~5μm aluminium layers, during the first stripping step, cause the pores of the first anodization to collapse and form dense clusters. These clusters then prevent the even etching of the alumina during the second stripping step, resulting in defects to the final alumina mask.

Partial stripping anodization and regular two-step anodization were both performed on graphene containing samples after optimization to compare the results. Neither technique showed exceptional results. Low adhesion between the aluminium and graphene layers caused delamination and bubbling issues during anodization that also disrupted the pore formation process. Patterning of the Mo into 10x10 mm areas prior to the CVD growth was attempted to improve adhesion of the aluminium layer on the outer region of the die. However, no perceptible

changes were observed to the severity of the delamination issues during anodization. Still, it was demonstrated that graphene and the Mo catalyst can survive the anodization process.

Plasma etching was done on both Al-on-Si test samples as well as graphene containing samples. With Al-on-Si, very positive results were observed. A cross-sectional SEM image showed that a sample with a mask fabricated with partial stripping two-step anodization, had notably even etch patterns underneath the pores after a very short 15 seconds SF6 based etching. This success was attributed mostly to the good adhesion between the layers and the pore widening step that is included in the partial stripping anodization process. When another Al-on-Si sample was tested with a regular two-step anodization fabricated alumina mask, around 10 minutes were needed for the plasma to pierce through the bottom of the pores of the alumina layer, and the resulting etching patterns were very uneven and varying in depth.

With graphene containing samples, plasma etching showed limited success. On the areas where the mask had not endured severe delamination, etching patterns on the graphene likely corresponding to the pores were observed. On the areas closer to the centre of the die where delamination was worse, however, no etch marks were observed. In summary, while promising progress was made toward the fabrication of graphene nanomesh using a transfer-free anodization process, challenges related to material adhesion and mask stability remain.

5.1 Future work

As outlined in the conclusions, the primary challenge in fabricating graphene nanomeshes using nanoporous alumina as a mask was poor adhesion. To address this and other issues, several potential avenues for future work are proposed:

· **Smaller patterned areas of Mo:** Just like it was tried already in this thesis, the Mo layer can be patterned to have areas on the die where the aluminium sits directly on top of the silicon to improve adhesion. However, this could be taken one step further by severely reducing the area of the patterned Mo. Making very small Mo island scattered throughout the die would make delamination highly unlikely for the mask regions above the graphene.

· **AAO as etching mask for Mo:** Another approach to improve adhesion would involve changing the order of steps of the overall process. Instead of etching with anodized alumina (AAO) on graphene, etching could first be performed on the Mo layer before the graphene CVD growth process is done. Anodization and etching would work adequately thanks to the better adhesion, and then graphene could be grown on the patterned Mo once the AAO mask is removed.

· **Replacing stripping solution:** Replacing sodium molybdate with chromic acid in the stripping solution could improve the process. With the use of chromic acid, there would be no need to use partial stripping, and two step process could be performed with thicker aluminium layers, resulting in higher pore ordering of the mask.

· **Trying alternative electrolytes:** Using different electrolyte solutions in the anodization process would yield variations in pore size of the alumina mask. Producing graphene nanomeshes with different morphologies would be interesting to explore once the adhesion issues are solved.

6 BIBLIOGRAPHY

[1] A. K. Geim and K. S. Novoselov, “The rise of graphene,” *Nature Materials 2007 6:3*, vol. 6, no. 3, pp. 183–191, Mar. 2007, doi: 10.1038/NMAT1849.

[2] I. Meric, M. Y. Han, A. F. Young, B. Ozyilmaz, P. Kim, and K. L. Shepard, “Current saturation in zero-bandgap, top-gated graphene field-effect transistors,” *Nat Nanotechnol*, vol. 3, no. 11, pp. 654–659, 2008, doi: 10.1038/nnano.2008.268.

[3] X. Li, X. Wang, L. Zhang, S. Lee, and H. Dai, “Chemically derived, ultrasmooth graphene nanoribbon semiconductors,” *Science*, vol. 319, no. 5867, pp. 1229–1232, Feb. 2008, doi: 10.1126/SCIENCE.1150878.

[4] L. Jiao, L. Zhang, X. Wang, G. Diankov, and H. Dai, “Narrow graphene nanoribbons from carbon nanotubes,” *Nature*, vol. 458, no. 7240, pp. 877–880, Apr. 2009, doi: 10.1038/NATURE07919.

[5] L. Liao *et al.*, “High-κ oxide nanoribbons as gate dielectrics for high mobility top-gated graphene transistors,” *Proc Natl Acad Sci U S A*, vol. 107, no. 15, pp. 6711–6715, Apr. 2010, doi: 10.1073/PNAS.0914117107/SUPPL_FILE/PNAS.0914117107_SI.PDF.

[6] X. Wang and H. Dai, “Etching and narrowing of graphene from the edges,” *Nature Chemistry 2010 2:8*, vol. 2, no. 8, pp. 661–665, Jun. 2010, doi: 10.1038/nchem.719.

[7] W. Lu and C. M. Lieber, “Nanoelectronics from the bottom up,” *Nat Mater*, vol. 6, no. 11, pp. 841–850, 2007, doi: 10.1038/NMAT2028.

[8] J. Bai, X. Zhong, S. Jiang, Y. Huang, and X. Duan, “Graphene nanomesh,” *Nature Nanotechnology 2010 5:3*, vol. 5, no. 3, pp. 190–194, Feb. 2010, doi: 10.1038/NNANO.2010.8.

[9] A. Sinitskii and J. M. Tour, “Patterning graphene through the self-assembled templates: Toward periodic two-dimensional graphene nanostructures with semiconductor properties,” *J Am Chem Soc*, vol. 132, no. 42, pp. 14730–14732, Oct. 2010, doi: 10.1021/JA105426H/ASSET/IMAGES/LARGE/JA-2010-05426H_0003.JPEG.

[10] X. Liang *et al.*, “Formation of bandgap and subbands in graphene nanomeshes with sub-10 nm ribbon width fabricated via nanoimprint lithography,” *Nano Lett*, vol. 10, no. 7, pp. 2454–2460, Jul. 2010, doi: 10.1021/NL100750V.

[11] Z. Zeng *et al.*, “Fabrication of graphene nanomesh by using an anodic aluminum oxide membrane as a template,” *Advanced Materials*, vol. 24, no. 30, pp. 4138–4142, Aug. 2012, doi: 10.1002/ADMA.201104281.

[12] A. Ruiz-Clavijo, O. Caballero-Calero, and M. Martín-González, “Revisiting anodic alumina templates: From fabrication to applications,” 2021, *Royal Society of Chemistry*. doi: 10.1039/d0nr07582e.

[13] O’SULLIVAN JP and WOOD GC, “Morphology and mechanism of formation of porous anodic films on aluminum,” *Proc Roy Soc Ser A Math Phys Sci*, vol. 317, no. 1731, 1970, doi: 10.1098/RSPA.1970.0129.

[14] K. Shimizu, K. Kobayashi, G. E. Thompson, and G. C. Wood, “Development of porous anodic films on aluminium,” *Philosophical Magazine A: Physics of Condensed Matter, Structure, Defects and Mechanical Properties*, vol. 66, no. 4, pp. 643–652, 1992, doi: 10.1080/01418619208201581.

[15] L. N. Sacco and S. Vollebregt, “Overview of Engineering Carbon Nanomaterials Such As Carbon Nanotubes (CNTs), Carbon Nanofibers (CNFs), Graphene and Nanodiamonds and Other Carbon Allotropes inside Porous Anodic Alumina (PAA) Templates,” Jan. 01, 2023, *MDPI*. doi: 10.3390/nano13020260.

[16] S. Ono, M. Saito, M. Ishiguro, and H. Asoh, “Controlling Factor of Self-Ordering of Anodic Porous Alumina,” *J Electrochem Soc*, vol. 151, no. 8, p. B473, 2004, doi: 10.1149/1.1767838/META.

[17] K. Nielsch, J. Choi, K. Schwirn, R. B. Wehrspohn, and U. Gösele, “Self-ordering Regimes of Porous Alumina: The 10% Porosity Rule,” *Nano Lett*, vol. 2, no. 7, pp. 677–680, 2002, doi: 10.1021/NL025537K.

[18] T. Yanagishita, M. Ozaki, and R. Kawato, “Fabrication of Gold Nanodot Array Using Anodic Porous Alumina as an Evaporation Mask Preparation of Ordered Porous Alumina Through-Hole Membranes with Large Hole Periods by Two-Layer Anodization,” 1996.

[19] H. Masuda, F. Hasegwa, and S. Ono, “Self-Ordering of Cell Arrangement of Anodic Porous Alumina Formed in Sulfuric Acid Solution,” *J Electrochem Soc*, vol. 144, no. 5, pp. L127–L130, May 1997, doi: 10.1149/1.1837634.

[20] H. Masuda, K. Yada, and A. Osaka, “Self-ordering of cell configuration of anodic porous alumina with large-size pores in phosphoric acid solution,” *Japanese Journal of Applied Physics, Part 2: Letters*, vol. 37, no. 11 PART A, Nov. 1998, doi: 10.1143/JJAP.37.L1340.

[21] V. Vega *et al.*, “Unveiling the Hard Anodization Regime of Aluminum: Insight into Nanopores Self-Organization and Growth Mechanism,” *ACS Appl Mater Interfaces*, vol. 7, no. 51, pp. 28682–28692, Dec. 2015, doi: 10.1021/ACSAMI.5B10712.

[22] Y. Li, M. Zheng, L. Ma, and W. Shen, “Fabrication of highly ordered nanoporous alumina films by stable high-field anodization,” *Nanotechnology*, vol. 17, no. 20, pp. 5101–5105, Oct. 2006, doi: 10.1088/0957-4484/17/20/010.

[23] F. Li, L. Zhang, and R. M. Metzger, “On the Growth of Highly Ordered Pores in Anodized Aluminum Oxide,” *Chemistry of Materials*, vol. 10, no. 9, pp. 2470–2480, 1998, doi: 10.1021/CM980163A.

[24] G. D. Sulka and K. G. Parkoła, “Temperature influence on well-ordered nanopore structures grown by anodization of aluminium in sulphuric acid,” *Electrochim Acta*, vol. 52, no. 5, pp. 1880–1888, Jan. 2007, doi: 10.1016/J.ELECTACTA.2006.07.053.

[25] M. Pashchanka and J. J. Schneider, “Self-ordering regimes of porous anodic alumina layers formed in highly diluted sulfuric acid electrolytes,” *Journal of Physical Chemistry C*, vol. 120, no. 27, pp. 14590–14596, Jul. 2016, doi: 10.1021/ACS.JPCC.5B11801.

[26] S. Akiya, T. Kikuchi, S. Natsui, and R. O. Suzuki, “Nanostructural characterization of large-scale porous alumina fabricated via anodizing in arsenic acid solution,” *Appl Surf Sci*, vol. 403, pp. 652–661, May 2017, doi: 10.1016/J.APSUSC.2017.01.243.

[27] O. Nishinaga, T. Kikuchi, S. Natsui, and R. O. Suzuki, “Rapid fabrication of self-ordered porous alumina with 10-/sub-10-nm-scale nanostructures by selenic acid anodizing,” *Sci Rep*, vol. 3, 2013, doi: 10.1038/SREP02748.

[28] W. J. Stępniowski, M. Moneta, M. Norek, M. Michalska-Domańska, A. Scarpellini, and M. Salerno, “The influence of electrolyte composition on the growth of nanoporous anodic alumina,” *Electrochim Acta*, vol. 211, pp. 453–460, Sep. 2016, doi: 10.1016/J.ELECTACTA.2016.06.076.

[29] Y. Hernandez *et al.*, “High-yield production of graphene by liquid-phase exfoliation of graphite,” *Nature Nanotechnology 2008 3:9*, vol. 3, no. 9, pp. 563–568, Aug. 2008, doi: 10.1038/nnano.2008.215.

[30] L. Zhu, X. Zhao, Y. Li, X. Yu, C. Li, and Q. Zhang, “High-quality production of graphene by liquid-phase exfoliation of expanded graphite,” *Mater Chem Phys*, vol. 137, no. 3, pp. 984–990, Jan. 2013, doi: 10.1016/J.MATCHEMPHYS.2012.11.012.

[31] J. Xu *et al.*, “Liquid-phase exfoliation of graphene in organic solvents with addition of naphthalene,” *J Colloid Interface Sci*, vol. 418, pp. 37–42, Mar. 2014, doi: 10.1016/J.JCIS.2013.12.009.

[32] A. Ciesielski and P. Samorì, “Graphene via sonication assisted liquid-phase exfoliation,” *Chem Soc Rev*, vol. 43, no. 1, pp. 381–398, Jan. 2014, doi: 10.1039/C3CS60217F.

[33] Q. Yu, J. Lian, S. Siriponglert, H. Li, Y. Chen Δ, and S.-S. Pei, “Graphene Synthesis by Surface Segregation on Ni and Cu”.

[34] S. Xu, L. Zhang, B. Wang, and R. S. Ruoff, “Chemical vapor deposition of graphene on thin-metal films,” *Cell Rep Phys Sci*, vol. 2, no. 3, p. 100372, Mar. 2021, doi: 10.1016/J.XCRP.2021.100372.

[35] S. S. Shams, R. Zhang, and J. Zhu, “Graphene synthesis: A Review,” *Materials Science-Poland*, vol. 33, no. 3, pp. 566–578, Sep. 2015, doi: 10.1515/MSP-2015-0079.

[36] Y. L. Zhong, Z. Tian, G. P. Simon, and D. Li, “Scalable production of graphene via wet chemistry: Progress and challenges,” *Materials Today*, vol. 18, no. 2, pp. 73–78, Mar. 2015, doi: 10.1016/j.mattod.2014.08.019.

[37] S. Stankovich *et al.*, “Synthesis of graphene-based nanosheets via chemical reduction of exfoliated graphite oxide,” *Carbon N Y*, vol. 45, no. 7, pp. 1558–1565, Jun. 2007, doi: 10.1016/J.CARBON.2007.02.034.

[38] W. S. Hummers and R. E. Offeman, “Preparation of Graphitic Oxide,” *J Am Chem Soc*, vol. 80, no. 6, p. 1339, Mar. 1958, doi: 10.1021/JA01539A017/ASSET/JA01539A017.FP.PNG_V03.

[39] S. Pei and H. M. Cheng, “The reduction of graphene oxide,” *Carbon N Y*, vol. 50, no. 9, pp. 3210–3228, Aug. 2012, doi: 10.1016/J.CARBON.2011.11.010.

[40] L. M. Malard, M. A. Pimenta, G. Dresselhaus, and M. S. Dresselhaus, “Raman spectroscopy in graphene,” *Phys Rep*, vol. 473, no. 5–6, pp. 51–87, Apr. 2009, doi: 10.1016/J.PHYSREP.2009.02.003.

[41] A. C. Ferrari and D. M. Basko, “Raman spectroscopy as a versatile tool for studying the properties of graphene,” *Nature Nanotechnology 2013 8:4*, vol. 8, no. 4, pp. 235–246, Apr. 2013, doi: 10.1038/nnano.2013.46.

[42] C. S. Cojocaru *et al.*, “Conformal anodic oxidation of aluminum thin films,” *Nano Lett*, vol. 5, no. 4, pp. 675–680, Apr. 2005, doi: 10.1021/NL050079B.

[43] “Engineering Basics: Guide to O-Rings | ERIKS shop NL.” Accessed: Aug. 31, 2024. [Online]. Available: https://shop.eriks.nl/en/guide-o-rings/

[44] M. C. (Department of Chemistry, Y. U. Z. T. (Kunming I. of Technology), M. C. (Department of Chemistry, and Y. U. Z. T. (Kunming I. of Technology), “A STUDY OF THE INHIBITIVE ACTION OF POTASSIUM CHROMATE ON ALUMINIUM IN PHOSPHORIC ACID,” *Journal of Chinese Society for Corrosion and protection*, vol. 8, no. 4, pp. 335–339, Oct. 2009.

[45] X. Li, S. Deng, and H. Fu, “Sodium molybdate as a corrosion inhibitor for aluminium in H3PO4 solution,” *Corros Sci*, vol. 53, no. 9, pp. 2748–2753, Sep. 2011, doi: 10.1016/J.CORSCI.2011.05.002.

[46] J. H. Lee *et al.*, “Large-Scale Fabrication of 2-D Nanoporous Graphene Using a Thin Anodic Aluminum Oxide Etching Mask,” *J Nanosci Nanotechnol*, vol. 13, no. 11, pp. 7401–7405, Nov. 2013, doi: 10.1166/JNN.2013.7876.

[47] S. Vollebregt, R. Ishihara, F. D. Tichelaar, Y. Hou, and C. I. M. Beenakker, “Influence of the growth temperature on the first and second-order Raman band ratios and widths of carbon nanotubes and fibers,” *Carbon N Y*, vol. 50, no. 10, pp. 3542–3554, Aug. 2012, doi: 10.1016/J.CARBON.2012.03.026.

[48] S. Tegen and P. Moll, “Etch Characteristics of Al[sub 2]O[sub 3] in ICP and MERIE Plasma Etchers,” *J Electrochem Soc*, vol. 152, no. 4, p. G271, 2005, doi: 10.1149/1.1865912.

[49] V. M. Donnelly and A. Kornblit, “Plasma etching: Yesterday, today, and tomorrow,” *Journal of Vacuum Science & Technology A: Vacuum, Surfaces, and Films*, vol. 31, no. 5, Sep. 2013, doi: 10.1116/1.4819316/244912.

7 Appendix

7.1 Process Flowchart

10x10 mm Mo patterns

FLOWCHART

CONTAMINATION: No

VERSION 3.3

Valid from March 2023

BATCH INFORMATION			
NAME OF OWNER :	Oscar Ortega Gonzalez	MASK SET :	General
NAME OF MENTOR :	Sten Vollebregt	MASK BOX :	Box 262
RUN NUMBER :	2024-15	DIE SIZE :	20x20mm
WAFER AMOUNT :	4	START DATE :	18.07.2022
SUBJECT TO PCC :		PCC APPROVED :	

DELFT UNIVERSITY OF TECHNOLOGY ELSE KOOI LABORATORY
Adress : Feldmannweg 17, 2628 CT Delft, The Netherlands
P.O. Box : 5053, 2600 GB Delft, The Netherlands
Phone : +31 - (0)15 - 2783868
Fax : +31 - (0)15 - 2622163
Website : www.tudelft.nl/ewi/onderzoek/faciliteiten/else-kooi-lab

Final structure

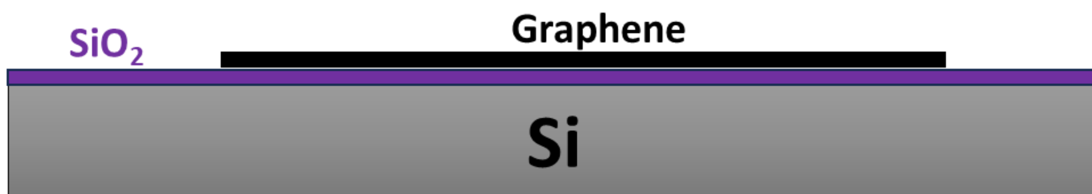

GENERAL RULES

CLEANROOM BEHAVIOUR

❶ Always follow the "**Security and Behavior**" rules when working in the EKL laboratories.
❷ Always handle wafers with care during processing. Use cleanroom gloves and work as clean as possible!
❸ Use cleanroom gloves when working with vacuum equipment. Do not touch the inside or carriers with bare hands.
❹ Always check equipment and process conditions before starting a process. Do **NOT** make unauthorized changes!
❺ Always follow the operating instructions from the system manuals when using machines.
❻ Directly notify the responsible staff member(s) when there are problems with the equipment (like malfunction or contamination). Flip the status card on the machine over to **DOWN** to warn other users. Also change the status of the system to **DOWN** in the "Phoenix Living Database" system.
❼ **DO NOT TRY TO REPAIR OR CLEAN EQUIPMENT YOURSELF**, and **NEVER** try to refresh a contaminated etch or cleaning bath! Only authorized staff members are allowed to do this.

WORKING WITH CMOS INCOMPATIBLE MATERIALS

❶ Substrates, layers and chemicals which are not CMOS compatible may cause contamination of bathes, equipment, wafer boxes, etc.. Using these materials in the class 100 and SAL cleanroom without permission is **FORBIDDEN.**
❷ The use of CMOS incompatible materials for processing in the class100 and SAL cleanroom must **ALWAYS BE EVALUATED** and **APPROVED** by your mentor and the EKL contamination officer.
❸ Wafers that are contaminated may **NEVER** be processed in any of the bathes or equipment without permission. Special precautions may be required, like the use of a separate container, a special substrate holder or a wafer carrier.
❹ You **MUST** work according to the rules described in the **Preventive Cross Contamination** (PCC) document, available on the "EKL Sharepoint webpage", and the **Materials** database from the "Phoenix Living Database" system.

CLEANING OF WAFERS

Wafers must always be cleaned before performing a **COATING, FURNACE, EPITAXY** or **DEPOSITION** step if they were stored for 4 hours or more.

Use the correct cleaning bathes:

- Acetone ⇨ To remove photoresist that is not used as a mask for ion implantation or plasma etching.
- Tepla stripper ⇨ To remove ion bombarded photoresist after implantion or plasma etching.
- HNO_3 99% (Si)$^+$ ⇨ For importing wafers that were processed outside the class100 or SAL cleanroom, and that were **not** in contact with metal layers. **APPROVAL** for importing is needed.
- HNO_3 99% (Si) ⇨ To remove organic material from wafers which were not in contact with metal layers.
- HNO3 69.5% (Si) ⇨ To remove (possible) metal particles caused by wafer handling. It is **NEVER** allowed to use this bath for wet etching or stripping of metal layers!

- HNO_3 99% (green metals)+ ⇨ For importing wafers that were processed outside the class100 or SAL cleanroom, and that were in contact with "green" metals. **APPROVAL** for importing is needed.
- HNO_3 99% (green metals) ⇨ To remove organic material on wafers which are or have been in contact with "green" metals (e.g.: Al, Al(1%Si), Ti, Mo, Zr, ...).

Note:
- The above described cleaning procedures are only valid for CMOS compatible wafers with CMOS compatible materials on them. **For all other wafers follow the PCC rules and check the Phoenix Materials database.**
- Wafers do **NOT** have to be cleaned **after** a furnace, epitaxy or deposition step if the next process step will be performed immediately, unless the wafers are covered with particles.

FURNACE RESTRICTIONS

Wafers that are covered with photoresist or a metal layer may **NEVER** be processed in any of the furnaces. This also applies for wafers from which a metal layer has been removed by etching. Only alloying in tube C4 is allowed for wafers with an aluminium layer.

MEASUREMENTS

Always perform all the measurement and inspection steps, and **write down the results in your journal and in the logbooks that can be found at some of the equipment**. The results are used to monitor the processes and/or equipment.

It is possible to measure directly on your (CMOS compatible) process wafers with the following Class 100 equipment:

- The FR-scanner (reflectometer), the WOOLLAM and the KEYENCE microscope. The first 2 systems are used for thickness measurements of transparent layers, and the third system is used for 3D surface metrology. The measurements are non-destructive and without contact to the wafer surface.
- The Dektak 8 surface profilometer. This system is used for step height measurements. In this case a needle will physically scan over the wafer surface, which can be destructive for structures. It is a contact measurement.
- The Hitachi SEM. They can be used for inspection of your wafers and for width, depth or thickness measurements.

Note:
- After certain measurements **cleaning of your wafers** may be required for further processing.
- An extra wafer must be processed when other measurements are required (like sheet resistance and junction depth measurements). These wafers can not be used for further processing.

STARTING MATERIAL

Use **SINGLE SIDE** polished **LOW RESISTIVITY (L_{RES})** wafers, with the following specifications:

Type: p

Orientation: <100>

Resistivity: 1-5 Ωcm

Thickness: 525 ± 15 µm

Diameter: 100 mm

The process consists of 9 parts:

Part 1: Cleaning step (only if wafers are taken from an open box)
Part 2: Creation of alignment marks
Part 3: PECVD oxide deposition
Part 4: Metal deposition
Part 5: Lithography
Part 6: Metal etching
Part 7: Metal fence removal
Part 8: Cleaning step
Part 9: Passivation

1. CLEANING: HNO3 99% and 69.5%

Perform this step ONLY when wafers are taken out of an already opened box!

Clean: 10 minutes in fuming nitric acid at ambient temperature. This will dissolve organic materials. Use wet bench "HNO_3 99% (Si)" and the carrier with the white dot.

Rinse: Rinse in the Quick Dump Rinser with the standard program until the resistivity is 5 MΩ.

Clean: 10 minutes in concentrated nitric acid at 110 °C. This will dissolve metal particles. Use wet bench "HNO_3 69,5% 110C (Si)" and the carrier with the white dot.

Rinse: Rinse in the Quick Dump Rinser with the standard program until the resistivity is 5 MΩ.

Dry: Use the "Avenger Ultra-Pure 6" rinser/dryer with the standard program, and the white carrier with a red dot.

2. OXIDATION

Furnace no: C1 or D1 Program name: WET1000

PROCESS	TEMPERATURE (in °C)	GASSES & FLOWS (in liter/min)	TIME (in minutes)	REMARKS
boat in	600	nitrogen: 6.0	5	
stabilize	600	nitrogen: 6.0	10	
anneal	600	nitrogen: 6.0	15	
heat up	+10 °C/min	nitrogen:3.0 oxygen: 0.3	40	
stabilize	1000	nitrogen:3.0 oxygen: 0.3	2	
oxidation	1000	oxygen: 2.25 hydrogen: 3.85	42	Target 300nm oxide thickness
cool down	-7 °C/min	oxygen: 2.25 hydrogen: 3.85	60	
boat out	600	nitrogen:3.0	5	

3. MEASUREMENT: OXIDE THICKNESS

Use the Woollam measurement system to measure the oxide thickness:

Oxide thickness: 300 nm on the process wafers

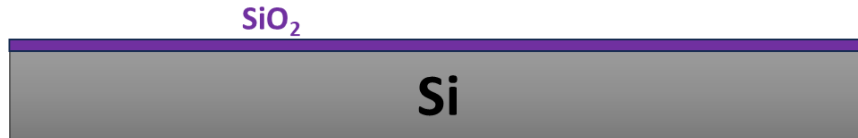

4. Mo DEPOSITION: 50nm

Use the TRIKON SIGMA sputter coater for the deposition of the catalyst metal Mo layer on the process and test wafers.

Follow the operating instructions from the manual when using this machine.

If necessary perform a target clean with recipe **'_Trgt_Cln_Mo_50C'**.

Use recipe '**Mo_50nm_50C**'.

Visual inspection: the metal layer must look shiny

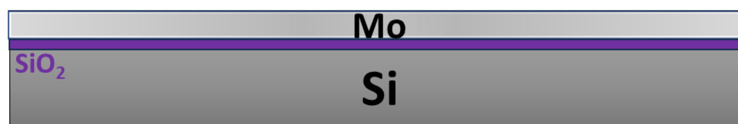

5. COATING

Use the coater station of the EVG120 system to coat the wafers with photoresist.

The process consists of a treatment with HDMS (hexamethyldisilazane) vapor with nitrogen as a carrier gas, spin coating with AZ NLOF2020 negative photoresist, and a soft bake at 95degC for 90 seconds.

Always check the temperature of the hotplate and the relative humidity (48 ± 2 %) in the room first.

Use coating "**Co – nlof2020 – 3,5um – no EBR**" (resist thickness 3.500um).

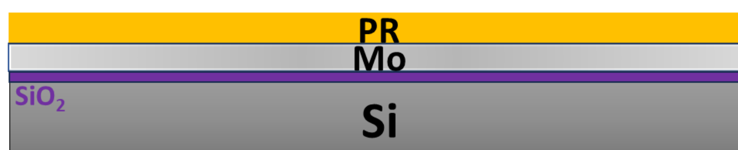

6. ALIGNMENT AND EXPOSURE

Processing will be performed on the
ASML PAS5500/80 automatic wafer stepper.

Expose **mask Open 10x10, box 262, Mask ID “A1”** with job **diesize_20mm/n20a-1, layer ID=1.**

If only g20a-1 exist follow the procedure to expose without alignment markers in the stepper manual

Use 88 mJ/cm^2, focus = 0.

7. DEVELOPING

Use the developer station of the EVG120 system to develop the wafers. The process consists of:

- a post-exposure bake at 115 °C for 90 seconds
- developing with Shipley MF322 with a single puddle process
- a hard bake at 100 °C for 90 seconds

Always follow the instructions for this equipment.

Use development program "**Only-X-link Bake**".
Use development program "**xDens-Dev-Lift-Off**".

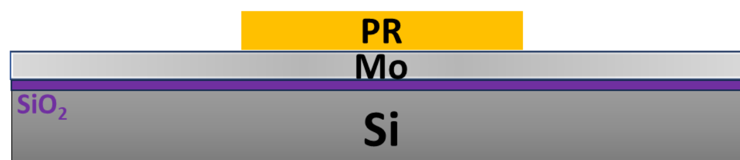

8. INSPECTION

Visually inspect the wafers through a microscope:

- No resist residues are allowed.
- Check the linewidth of the structures.
- Check the overlay of the exposed pattern if the mask was aligned to a previous pattern on the wafer.

PLASMA ETCHING OF Mo

Use the Trikon Ωmega 201 plasma etcher.

Follow the operating instructions from the manual when using this machine.

Check the etching time!

Use sequence **'Mo_TEST8'** and set the etching time to **t= ?? s**.

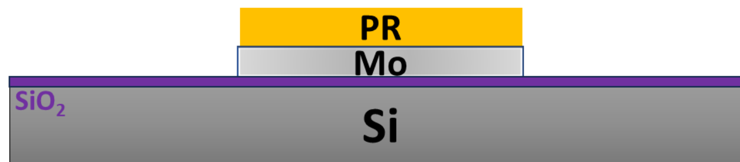

9. CLEANING PROCEDURE: TEPLA

Plasma strip:

- Use the Tepla plasma system to remove the photoresist in an oxygen plasma.
- Follow the instructions specified for the Tepla stripper, and use the quartz carrier.
- Use program 1
- In case if there is a problem with Tepla, use NI555 in SAL in an ultrasonic bath for 5-10 min.

Visual inspection: the metal layer (protected by the photoresist) must look shiny.

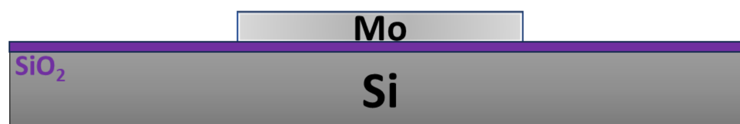

10. GRAPHENE GROWTH

Use the **AIXTRON BlackMagic Pro** to grow graphene using LPCVD at 935°C.

Use recipe '**Mo_NEW_935C_20min_CH4_20min_pre_annealing**'.

The process wafers are now considered Cu contaminated. Beware of which tweezers to use when handling the wafers. Put the wafers in a process box dedicated for Cu contaminated processes.

USE WHITE BLISTER WITH Cu WRITTEN ON IT

11. Aluminium deposition

Use the TRIKON SIGMA sputter coater for the deposition of the pure aluminium layer on the backside of the process wafers.

Follow the operating instructions from the manual when using this machine.

Make sure the pure Al target is installed.

Recipe pAl_XXXum_RT

Use a dedicated Cu carrier wafer!

7.2 Welch t-test

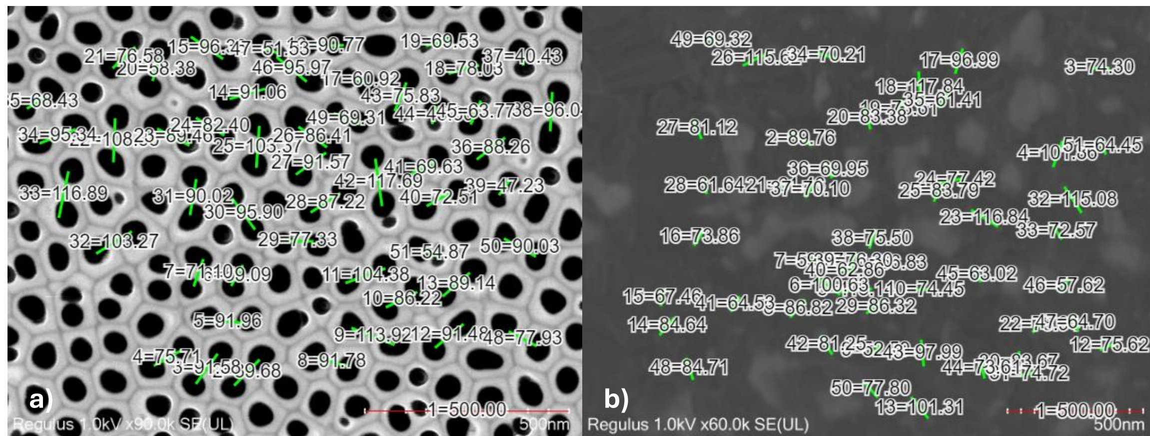

Figure 36: Top-view SEM images used to extract the measurements for the Welch test. (a) Top-view image of pores of alumina mask. (b) Top-view image of marks of etched graphene.

	Interpore distance of alumina (nm)	Distance between graphene etch marks (nm)		Interpore distance of alumina (nm)	Distance between graphene etch marks (nm)
1	89.68	89.76	**26**	91.57	81.12
2	91.58	74.3	**27**	87.22	61.64
3	75.71	101.86	**28**	77.33	86.32
4	91.96	118.14	**29**	95.9	83.67
5	59.09	100.63	**30**	90.02	74.72
6	71.1	59.57	**31**	103.27	115.08
7	91.78	86.82	**32**	116.89	72.57
8	113.92	52.59	**33**	95.34	70.21
9	86.22	74.45	**34**	68.43	61.41
10	104.38	66.83	**35**	88.26	69.95
11	91.48	75.62	**36**	40.43	70.1
12	89.14	101.31	**37**	96.04	75.5
13	91.06	84.64	**38**	47.23	76.3
14	96.38	67.46	**39**	72.51	62.86
15	90.77	73.86	**40**	69.63	64.53
16	60.92	96.99	**41**	117.69	81.25
17	78.03	117.84	**42**	75.83	97.99
18	69.53	73.61	**43**	45.3	73.61
19	58.38	83.38	**44**	63.77	63.02
20	76.58	61.46	**45**	95.97	57.62
21	108.35	78.94	**46**	51.53	64.7
22	89.46	116.84	**47**	77.93	84.71
23	82.4	77.42	**48**	69.31	69.32
24	103.37	83.79	**49**	90.03	77.8
25	86.41	115.62	**50**	54.87	64.45

Table 2: Distance between pores and graphene etch marks used as samples for the Welch t-test.

	Alumina interpore distance	*Graphene etch marks distance*
Mean	82.5996	79.8836
Variance	335.1715	286.6159
Observations	50	50
Hypothesized Mean Difference	0	
df	97	
t Stat	0.770183	
P(T<=t) one-tail	0.221532	
t Critical one-tail	1.660715	
P(T<=t) two-tail	0.443063	
t Critical two-tail	1.984723	

Table 3: Results of Welch t-test